HOKKAIDO UNIVERSITY

Title	Polaritonic Multi Electron Transfer Reactions Using Structured Electrodes
Author(s)	佐藤, 大樹
Degree Grantor	北海道大学
Degree Name	博士(理学)
Dissertation Number	甲第16365号
Issue Date	2025-03-25
DOI	https://doi.org/10.14943/doctoral.k16365
Doc URL	https://hdl.handle.net/2115/97627
Type	doctoral thesis
File Information	SATO_Daiki.pdf

Hokkaido University Collection of Scholarly and Academic Papers : HUSCAP

Polaritonic Multi Electron Transfer Reactions Using Structured Electrodes

構造電極によるポラリトン多電子移動反応制御

Daiki Sato

佐藤大樹

Graduate School of Chemical Sciences and Engineering
Hokkaido University
北海道大学大学院総合化学院
2025

Contents

1. General Introduction

1.1 Water Splitting

Currently, various alternative energy sources are being discussed with the goal of escaping fossil fuels. Renewable energy includes methods of generating electricity using wind and solar power, as well as nuclear power. There are also various types of energy carriers, one of them is hydrogen. Generating electric in some way, the electric energy is converted into chemical energy as hydrogen, then transporting and storing it. The one of the simplest methods of converting electrical energy into hydrogen energy is water splitting. During water splitting, oxygen is generated at the positive electrode and hydrogen is generated at the negative electrode, as shown in Fig. 1.1a.[1] Although thermodynamical principle predicts that the voltage difference between the two electrodes is 1.23 V (Fig. 1.1b), excess energy is required to proceed with the reaction at a certain rate, which is called as overpotential. The overpotential includes energy loss during electron transfer at the electrode interface, energy loss associated with material transfer when moving from the vicinity of the electrode to the electrode interface, and due to solution resistance, which behaves similarly to the resistance of an electric circuit. Most recent water splitting studies have focused on how to reduce these energy losses. Fig. 1.2 shows the overpotential required to reach to 10 mA cm^{-2} for various catalysts.[2] Research has been conducted on a wide range of pH solutions but the most notable are Pt, Ir, and Ru. These metals are highly active, but are also rare, so using these materials for industrial water splitting would require huge costs. Materials have an activity comparable to that of precious metal catalysts have also been developed using inexpensive alloys of nickel and iron and so on.

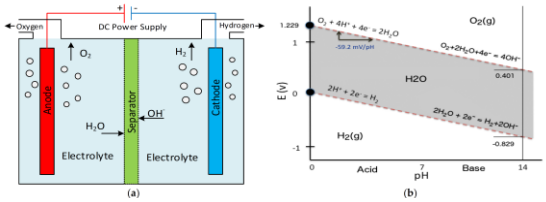

Figure. 1.1 (a) Schematic illustration of electrical process for water splitting system, (b) Pourbaix diagram for water.

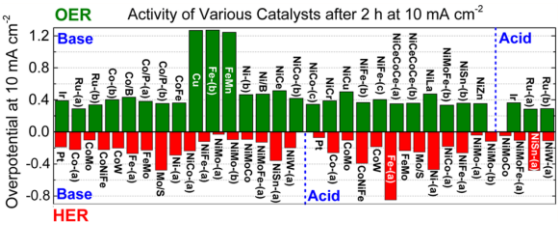

Figure. 1.2 Various catalysis and its overpotential for Oxygen Evolution Reaction and Hydrogen Evolution Reaction in acid and base electrolytes.

On the other hand, water splitting using light energy has also been studied in the past. Domen et al. have carried out large-area photochemical water splitting in outdoor tests using natural sunlight.[3] Furthermore, research has been conducted on water splitting using both electrical energy and light energy, where light energy was used to reduce iron ions and generate oxygen, and electrical energy in the other cell was used to oxidize iron ion and generate hydrogen. Here, the net balance before and after the reaction of iron ions was zero. The electrical energy used in this case was 0.9 V.[4]

1.2 Oxygen Evolution Reaction (OER)

Electrochemical OER is the anode (= positive electrode) reaction in the water splitting. In the recent trend of hydrogen society to realize carbon neutrality, OER cannot be ignored if the hydrogen source is water. The following five elementary reactions are considered in the OER.

$$M + H_2O \rightarrow MOH + H^+ + e^- \quad (1)$$

$$MOH \rightarrow MO^* + H^+ + e^- \quad (2)$$

$$MO^* + H_2O \rightarrow MOOH + H^+ + e^- \quad (3)$$

$$MOOH \rightarrow MOO^* + H^+ + e^- \quad (4)$$

$$MOO^* \rightarrow M + O_2 \quad (5)$$

OER proceeds through these elemental reactions. Currently, various electrode materials have been proposed, but the overpotentials are still large.[5]

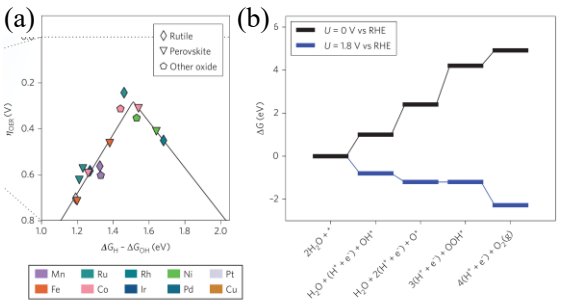

Figure. 1.3. (a) Overpotential volcano plot versus difference between H and OH adsorption energy of various catalysis for OER , (b) DFT calculation for OER elementary step.

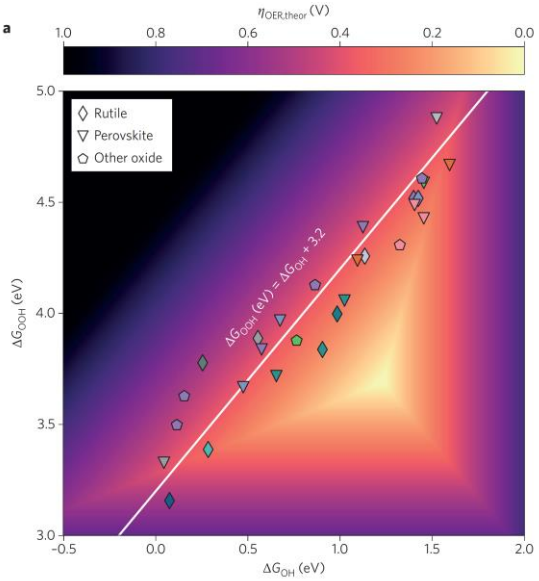

Figure. 1.4. 2D Volcano image for OER, OOH versus OH adsorption energy. White line indicates linear relation of OOH and OH adsorption energy.

According to theoretical calculations,[6] the important intermediates in OER are said to be MO* and MOOH (2nd or 3rd step of elementary reactions), and the step where MO* is generated from MOH or MOOH is generated by H_2O attack on MO* is said to determine the OER overpotential. Fig. 1.3 summarizes the overpotential of each metal oxide and the free energy change in each elementary reaction step. There is a large free energy difference in the MO* step between MOH and MOOH. In other words, the difference between ΔG_{OH} and ΔG_O represents the overpotential in many catalysts. In these metal oxide catalysts, a volcano-type relationship is observed. If ΔG_O is larger than ΔG_{OH} and smaller than ΔG_{OOH}, the overpotential is only about 0.3 V, which is on the top of volcano .

Fig. 1.4 shows a two-dimensional plot of the adsorption free energies of OH and OOH, ΔG_{OH} and ΔG_{OOH}. From this figure, the adsorption free energies ΔG_{OH} and ΔG_{OOH} follows linear relationship ($\Delta G_{OOH} = \Delta G_{OH} + 3.2 \pm 0.2$ [eV]), and it is completely located at the pale orange region showing desired optimum activity. To reduce the overpotential of the entire reaction, materials or catalysts design that breaks this linear relationship are needed .

There are various metals based OER catalysts, including chalcogenides (especially oxides), nitrides, and phosphides. Among them, oxides have attracted attention for the following reasons. (1) Metal

oxides are thermodynamically stable, inexpensive, and easier to produce commercially than other compounds. (2) In an oxidizing atmosphere and aqueous solution, non-oxidized metals are easily oxidized to produce oxides and hydroxides. (3) The oxidation numbers of metal oxides vary and can be changed depending on the structure and environment of the metal atom. As a result, the OER activity and stability can be tuned.

Currently, the absorbate evolution mechanism (AEM, Fig. 1.5a) and lattice oxygen mechanism (LOM, Fig. 1.5b) are proposed as possible mechanisms of OER.[7] In AEM, the source of O is only water. In contrast, in LOM, oxygen in the crystal is involved in the reaction mechanism, and this has been confirmed in experiments using ^{18}O. In LOM, the formation of O-O bonds occurs directly (lattice oxygen and water oxygen), so it is more advantageous than AEM in terms of kinetics and overpotential.[8] Because of that reason, this reaction mechanism has a potential to fall the over potential below its lower limit of 0.37 V in AEM, and the theoretical limit is 0. Actually, the overpotential can be reduced to 0.17 V. Furthermore, a shift in the volcano plot due to the transition of the reaction mechanism from AEM to LOM has been observed in the La perovskite system, suggesting the possibility of breaking through the theoretical limit in new materials. However, metal cations are generated due to oxygen defects during the LOM reaction. In this case, the rate at which oxygen defects are generated is faster than the rate at which they are filled, so the cations remain for a long time. These cations are very unstable and change to a higher oxidation number or dissolve into the solution, which causes the catalytic cycle stopping. In addition, the cations dissolved into the solution may form bonds with cation in the solution and deposit on the catalyst surface again, causing the surface to become amorphous and filling the active sites.

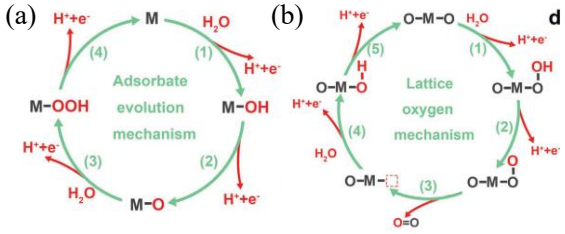

Figure. 1.5. OER molecular mechanisms of catalytic cycles, (a) AEM, (b) LOM.[7]

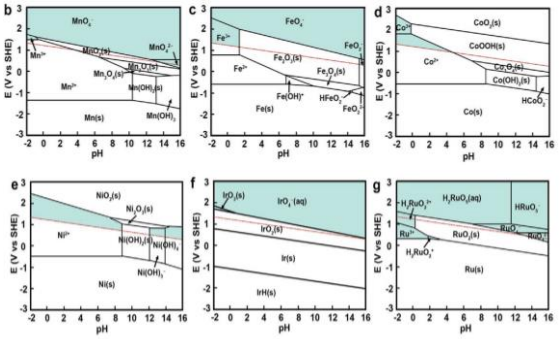

Figure. 1.6. Pourbaix diagram for various transition metal.

Stability under OER conditions is also an issue for metal oxide catalysts. Fig. 1.6 shows the Pourbaix diagrams of metals (Mn, Fe, Co, Ni, Ir, Ru) used as OER catalysts. Many metals form complex ions at potentials higher than 1.23 V, which means that there are limitations to the selection of materials even when searching for new materials, and there are limitations to the selection of materials using existing methods.

1.3 Hydrogen Evolution Reaction (HER)

HER is the cathode reaction of water splitting, and various studies have been conducted since it was reported by Tafel in 1905.[9] The half-reaction is generally written as equation below.

$$2H^+ + 2e^- \rightarrow H_2 \qquad (6)$$

There are three considerable elementary steps (Fig. 1.7): the Volmer step (discharge step), in which H^+ in the solution near the catalyst receives e^- and adsorbs onto the catalyst surface. The Heyrovsky step (electrochemical desorption step), in which adsorbed H on the catalyst surface receives e^- and combines with H^+ in the solution to produce H_2. The Tafel step (chemical desorption step), in which two adsorbed H on the catalyst surface combine to produce H_2.

First, the Volmer step proceeds, after that the reaction proceeds as the Heyrovsky step or the Tafel step.

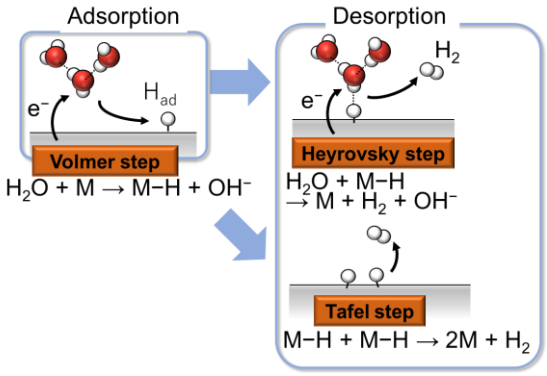

Figure 1.7. Schematic illustration of physicochemical molecular processes of HER on an electrode.

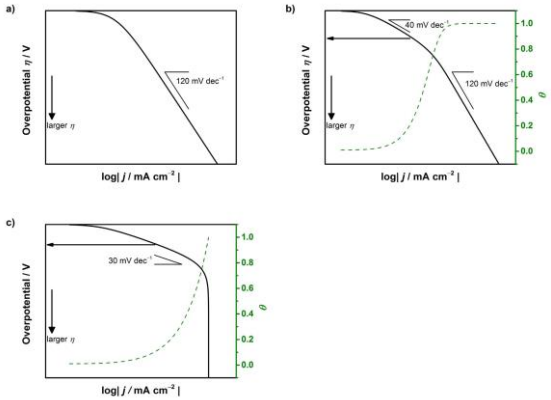

Figure 1.8. Theoretical Tafel plot for HER and coverage of electrode surface for its rate-determining step.

According to Tafel, when the logarithm of the current in the HER is plotted against the potential (it is called Tafel plot), almost all metals show a similar slope except for platinum, which has a smaller slope compared to other metals. The slope of the Tafel plot in HER usually indicates the rate-determining step, which is Volmer step at 120 mV dec^{-1}, Heyrovsky step at 40 mV dec^{-1} (in high potential 120 mV dec^{-1}), and Tafel step at 30 mV dec^{-1} (Fig. 1.8).[10]

Because H^+ is the reactant, the concentration of H^+ in the solution relying on the pH affects kinetics and activity of HER. In alkaline solutions with a very low H^+ concentration, the H^+ source is H_2O. The elementary reactions in an acidic solution are shown as follows, where M represents the adsorption site.

$$\text{Volmer step: } M + H^+ + e^- \rightarrow MH \qquad (7)$$

$$\text{Heyrovsky step: } MH + H^+ + e- \rightarrow H_2 \qquad (8)$$

$$\text{Tafel step: } 2MH \rightarrow H_2 \qquad (9)$$

In contrast, in an alkaline the processes are following:

$$\text{Volmer step: } M + H_2O + e^- \rightarrow MH + OH^- \qquad (10)$$

$$\text{Heyrovsky step: } MH + H_2O + e^- \rightarrow H_2 + OH^- \qquad (11)$$

$$\text{Tafel step: } 2MH \rightarrow H_2 \qquad (12)$$

In addition, in alkaline solutions, as can be seen from equation (10) or (11), the overpotential increases because additional energy is required to generate H^+ from H_2O (Fig. 1.9).[11] It was proposed that the Volmer step can be divided into more detailed categories based on the hydroxyl group adsorption properties of the catalyst surface. If it is easy that hydroxyl adsorption occurs on surfaces of catalysts (oxophilic), the reaction process is expressed as follows.

$$2M + H_2O \rightarrow MH + MOH \quad (13)$$

$$MH + MOH + e^- \rightarrow MH + OH^- \quad (14)$$

Alternatively, if it is difficult that hydroxyl adsorption occurs on surfaces of catalysts (oxophobic), the reaction process is expressed as follows.

$$M + H_2O + e^- \rightarrow MH + OH^- \quad (15)$$

As shown above, it can be predicted that the HER reaction rate on an oxophilic surface depends on the adsorption energy of OH and H. Markovic *et al*. have proposed a bifunctional mechanism in which H is adsorbed on Pt and OH is adsorbed on $Ni(OH)_2$, and the split H and OH are adsorbed on different types of active sites, based on the improvement in HOR and HER activity when $Ni(OH)_2$ is supported on Pt(111) compared to Pt(111).[12] In addition, in a solution of pH 13, The positions of Au and Cu are reversed in the volcano plot (Fig. 1.10a, b). If the bifunctional mechanism is used, it is clear that at pH 13, the adsorption of OH cannot be simply explained by the adsorption energy of H alone. This mechanism also explains the reversal of the HER activity of Au and Cu at pH 13 and pH 1 in terms of OH adsorption (Fig.

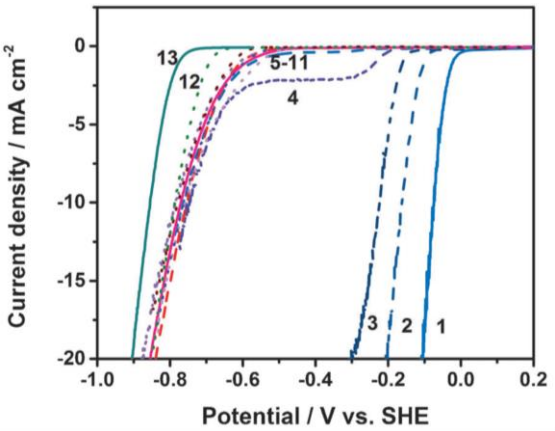

Figure 1.9. Current-potential curves for various pH, in three curves in right region H^+ react. Inserted numbers represent pH in solutions.

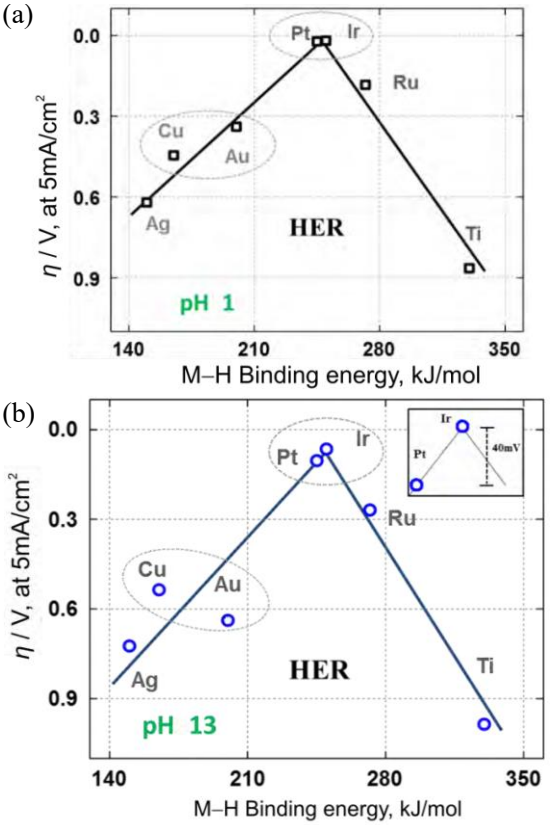

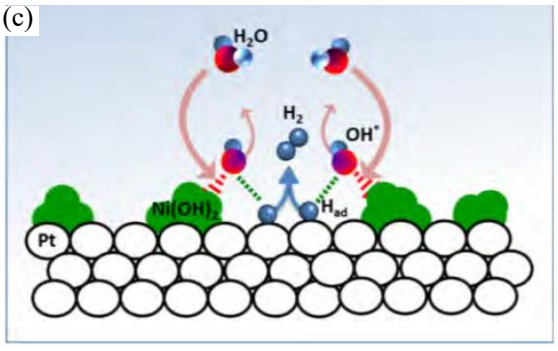

Figure. 1.10. (a) volcano plot in acid and (b) base, (c) proposed reaction of bifunctional mechanism.

1.10c). In other words, Cu is more likely to dissociate H and OH. The same thing happens between Pt and Ir. When comparing the activity of various metals with $Ni(OH)_2$, the reversal between Au and Cu disappears. By making OH adsorption site, the volcano plot of metal-$Ni(OH)_2$ at pH 13 approaches the volcano plot of the single metal at pH 1, strongly suggesting that H is adsorbed on the metal and OH is adsorbed on $Ni(OH)_2$.[13] It has also been found that when the metal that causes OH adsorption is $Ni(OH)_2$, $Co(OH)_2$, $Fe(OH)_2$, or $Mn(OH)_2$, the HER activity decreases depending on the strength of OH adsorption. In particular, it is thought that the activity decreases with Fe and Mn as adsorption energy between the metal and OH is too large, so that it is difficult for OH to be desorbed and catalysis cycle is slow.[14] In addition to the change in the reaction mechanism due to the pH change mentioned above, the change in the electric field at the electrode-solution interface is dependent on the pH. This results in a change in the energy of water reorganization on the electrode surface. In acidic solutions, the potential of zero charge (PZC) and maximum entropy potential (PME) are close to the region of hydrogen adsorption in underpotential deposition (UPD), whereas in basic solutions, the PZC and PME are very far from the hydrogen region. This is related to the fact that in basic solutions, a huge amount of energy is required for OH to pass through the electric double layer. Various experimental results support this. In fact, an experiment was conducted in which the pH-dependent overpotential was measured, and it was found that the HER overpotential increases as the base becomes higher. In other words, from the viewpoint of overpotential, the more base in the solution, the more disadvantage the HER becomes .[15] When this was investigated by impedance measurement, it was shown that H adsorption is slower in base solutions not only in the overpotential deposition (OPD) region but also in the UPD region. Furthermore, when the Tafel plots were taken for the Pt electrode at pH 1 and pH 13 and the electrode combining Pt and $Ni(OH)_2$ at pH 13, the slope was 120 mV dec^{-1} for the Pt electrode at pH 13, and about 40 mV dec^{-1} for the Pt/$Ni(OH)_2$ electrode at pH 1 and pH 13.[15] From this, the rate-determining step of the reaction elementary step changes in the bifunctional mechanism even if the pH is the same. Furthermore, when comparing the hydrogen

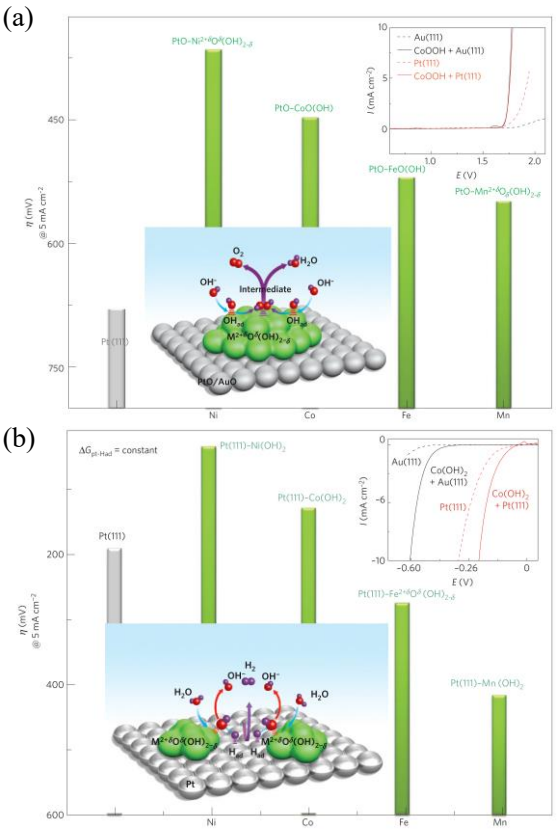

Figure. 1.11. (a) OER activity order in Pt/Ni or Pt/Co, Pt/Fe, Pt/Mn and OER molecular mechanism. (b) HER activity order in Pt/Ni or Pt/Co, Pt/Fe, Pt/Mn and HER bifunctional molecular mechanism.

adsorption charge transfer rate in the UPD region of H, it is clear that adsorption rate is higher in Pt and Pt/Ni $(OH)_2$ at pH 13 than in Pt/Ni $(OH)_2$. As another evidence, a correlation was found between the OER and HER activities of Pt supported with Ni, Co, Fe, and Mn, which are OER active catalysts. This suggests that OH adsorption is also important for HER in alkaline solutions (Fig. 1.11).[14]

On the other hands, ions such as K^+, Cs^+, and Li^+, which are used as so-called supporting electrolytes, do not react directly with HER, but some of them promote or inhibit the approach of H^+ to the electrode surface (Fig. 1.12a).[16] According to these results, the promotion or inhibition effect of HER also depends on the cation type and concentration, e.g., K^+ promotes the HER as the concentration increases at low concentrations but show inhibition at high concentrations. In the HER under acidic conditions, protons react directly, so the cation dependence does not emerge. In contrast, in the HER in alkaline solutions, H_2O is reduced, so the state of water solvated with the cation becomes important. Focusing on the acidity of the cation, Koper *et al*., investigated monovalent cations (Li^+, Cs^+) to trivalent cations (Al^{3+}, Nd^{3+}), and found that there was a clear selectivity for CO_2 reduction and H_2O reduction.[17] In Fig. 1.12b, MD calculations were also included, and the dependence of the distance to the outer Helmholtz layer formed by H_2O and the dissociation energy of HO-H, which depend on the acidity of the cation, was also discussed. On the other hand, it is known that the cation effect in alkaline solutions depends on the electrode material. For monovalent cations, the order is $Li^+ < Na^+ < K^+ < Cs^+$ for noble metals (Cu, Ag, Au), whereas the order is $Li^+ > Na^+ > K^+ > Cs^+$ for platinum group metals (Ir, Pd, Pt), showing the opposite trend. Fig. 1.12c.[18] The presence of cations reduces the intermediate energy in both noble metal and platinum group metal. The degree of reduction is smallest for Li^+ and largest for Cs^+. However, for platinum group metals, which originally had suitable intermediate energy, the free energy change increases. So, activation energy is required higher. As a result, it is thought that

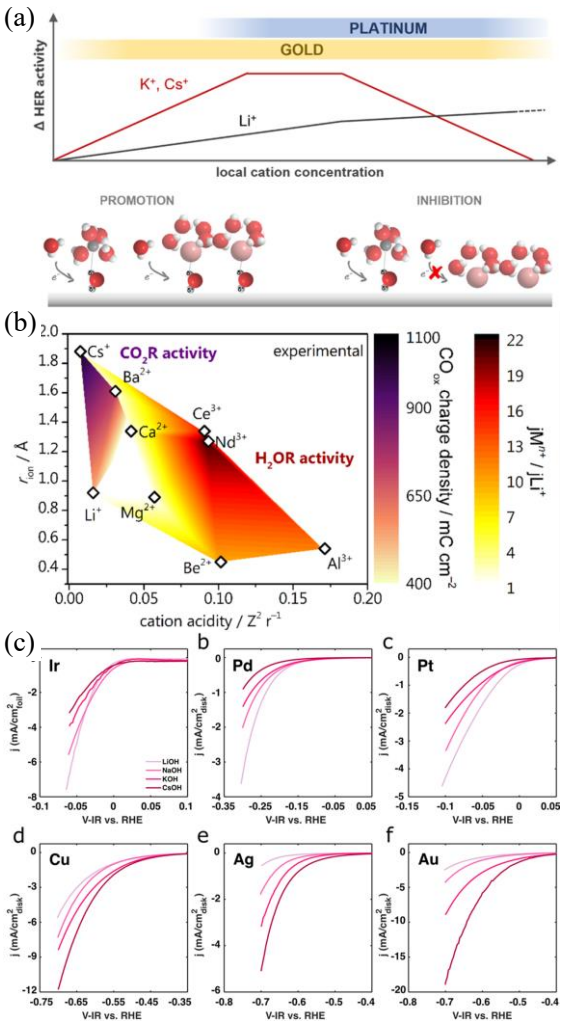

Figure. 1.12. (a) HER activity in base solution with cation concentration on Pt or Au electrode[16], (b) higher charge cation effect in HER and CO_2 reduction and 2D image of activity with cation radius and acidity, (c) cation effect on noble metals and platinum group metals. These have inverse trend because the difference of surface energy.

Cs^+ has the smallest activation energy among noble metals, while Li^+ has the smallest activation energy among platinum group metals.

There are also articles that discuss the interaction between hydrogen (proton) and metal surfaces, and the first example is the famous volcano plot based on Sabatier's principle. However, in the early reports, only the binding energy between hydrogen and metal surfaces have been discussed. After that, various theoretical calculations showed that a good catalyst requires the following three things.[19]

- According to Sabatier's principle, the free energy change of adsorption is 0.
- The Fermi level exists within the d band.
- The d band of the metal has a strong interaction with the 1s orbital of hydrogen over a wide range.

The wide range is quite severe, and the electron transfer to hydrogen is about 0.5 Å.

From these viewpoints, most metals can be classified into three groups. They are sp metals, coinage metal group, and d metals. The first sp metal group includes metals such as Pb and Hg, and the d band exists at a low energy level. Therefore, the interaction of the d band with the s orbital of hydrogen is very small, making it difficult to adsorb and desorb hydrogen. In the next coinage metal group, the d band does not exist at the Fermi level, but it exists at a nearby 1s orbital of hydrogen. From these factors, the change in the free energy of hydrogen adsorption is small. However, the spatial extent of the d band is small, so the interaction with the 1s orbital of hydrogen is small. Therefore, the rate of HER is small. Finally, the d metal group is explained by the fact that the d band is located near the Fermi level, except for Ni and Co. Among them, they can be divided into two types: those that cause UPD and others cause OPD depending on the degree of mutual adoption with hydrogen atoms, but metals cannot be simply classified into either type. Ni is one of the metals whose surface has a close-packed structure and causes spin polarization. Many metals with a close-packed surface and spin polarization eliminate the 1s spin polarization of hydrogen at about 2.4 Å. In contrast, in Ni, it disappears at 0.9 Å, so the spin polarization of Ni and H can interact, making it highly active. As mentioned above, even if it is simply discussed about the interaction between hydrogen and the metal surface, also it is necessary to consider each other's orbits and their spins, etc. Various factors are involved in HER. Until now, it has not unveiled what interaction affects to what extent yet. Because of the above, we are not yet at the stage to discuss overall so that we need to discuss each interaction carefully.

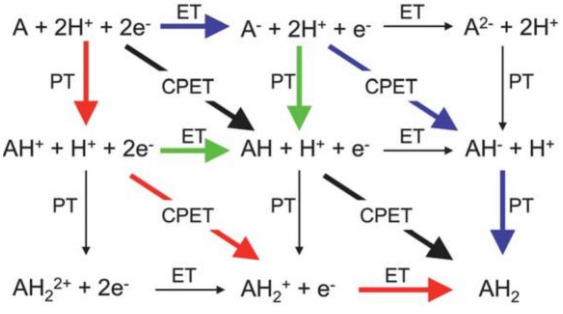

Figure. 1.13. Reaction pathways of HER, considering concerned of proton and electron transfer or decoupled pathways (now A is Metal and last A-H2 bond strength is zero).

In chemical reactions, the change of Gibbs free energy is an important factor. Applying this to multi-electron transfer reactions to optimieze catalysis, conditions that the change of free

energy in each step is nearly zero are necessary. In case of HER, reaction pathways are shown in Fig. 1.13. In proton coupled electron transfer (PCET), there are concerned reactions or decoupled reactions of proton and electron. In a concerned reaction, electron transfer (ET) and proton transfer (PT) occur at the same time. That is called concerned proton-electron transfer (CPET). On the contrary, in a decoupled reaction stepwise processes of ET and PT occur. In detail, there is a pathway in which ET proceeds first and PT proceeds later or reverse of it. The energy level of the intermediates in these three pathways are different. This is the situation in the first step and similar pathways exist in the second step. Because of the above reason, an ideal catalysis is needed to have the free energy changes of all intermediates which are close to zero. However, considering concerned and decoupled pathways and due to various factors, for example different charges, it is very difficult to develop optimal catalysis. In a particular catalysis, the reaction may proceed along the lower free energy changed path, but the above discussion is based on only thermodynamics and does not discuss kinetics. From this perspective, multi-electron, multi-proton reactions are complex reactions.

1.4 Quantum effect

The difference between H and D is one neutron, but the difference of mass is twice. So that Hydrogen is sensitive element for isotope effect. As shown in Fig. 1.14,[20] there is a difference in zero-point energy between H and D, so D_2O has a slower reaction rate than H_2O. Therefore, when a mixture is reacted, there is a clear difference in the reaction rate between H_2O and D_2O. The HER in a mixture of H_2O and D_2O has been investigated for a long time, and the separation factor (S_D), expressed by the following formula, has long been a subject of interest in the mixture.[21]

$$S_D = \frac{dH/H}{dD/D} = \frac{([H]/[D])_g}{([H]/[D])_l} \quad (16)$$

In the above formula, [H] and [D] are the concentrations of hydrogen and deuterium, and the subscripts g and l indicate the gas and liquid states, respectively.

In 1975, Enyo reported that the HER of Pt, Au, separation factor was determined using a Ni electrode.[22] The results confirmed that the S_D increases with increasing overpotential, and it was reported that hydrogen (H_2) is mainly produced when the overpotential is large because of changing of mechanism with overpotential.

In previous research in our laboratory,[23] it was

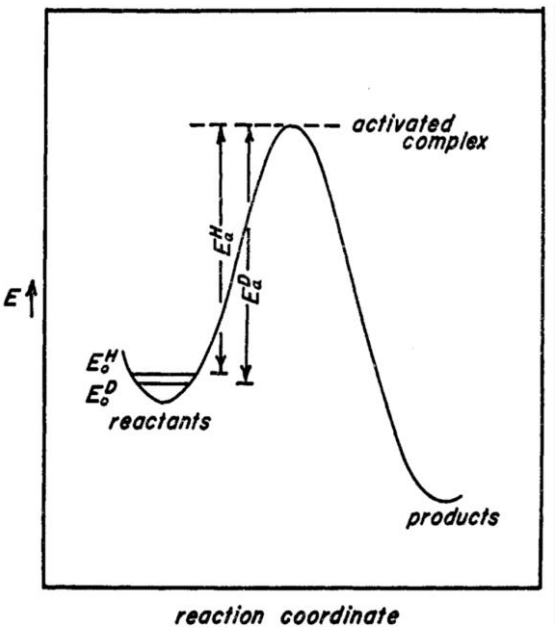

Figure. 1.14. Schematic diagram of the reaction coordinate of H and D.

known that the S_D ratio responds sensitively to factors such as the geometric structure of the electrode surface and the mixture ratio, and there are many unclear points regarding the factors that can achieve arbitrary S_D control.

In the isotope effect, equilibrium isotope effect (EIE) and kinetic isotope effect (KIE) are discussed. EIE is a thermodynamic effect involving the bond strength of hydrogen and oxygen in zero-point vibration. The equilibrium changes due to isotope substitution, which changes the standard potential of PCET.[24] On the other hand, KIE is about the reaction rate, and since it depends on the reaction mechanism and the nature of the transition state, it is evidence that the transfer of hydrogen and oxygen atoms is the rate-determining step. In this case, there are two possibilities: the transfer of hydrogen and electrons is stepwise or concerted. In stepwise PCET, if the proton transfer proceeds quickly and the electron transfer limits the reaction rate, KIE is not observed regardless of the nature of the proton (H or D). However, it is thought that KIE is observed if the proton transfer restricts the reaction rate. On the other hand, in concerted PCET, tunneling between the two bodies is required for both electron and proton transfer. Considering that the reaction proceeds through a transition state with a high energy, concerted PCET is an energetically suitable reaction mechanism. Experimental studies have shown that in stepwise PCET, the reaction rate is inverse proportional to the difference in the acid dissociation constant between the two substances. In other words, when the difference in the acid dissociation constant is large, the concerted reaction becomes relatively favorable. And because the acid dissociation constants of heavy water and light water are different, KIE is observed, which has a strong influence in stepwise PCET.

The relative position of the zero-point vibration level changes in the equilibrium between the reactants and the products. Also, EIE does not depend only on the energy of the zero-point vibration, but can be divided into the translation, rotation, vibration, etc. of the molecule. According to this way of thinking, it is expressed by the following formula.

$$\mathrm{EIE} = \mathrm{SYM} \times \mathrm{MMI} \times \mathrm{EXC} \times \mathrm{ZPE} \qquad (17)$$

SYM represents the number of symmetries of the molecule, and MMI represents the moment of inertia. EXC is the excitation term that takes into account the vibration, and ZPE is the energy of the zero-point vibration.

When PCET in quantum tunneling effect progresses, the wave function at the vibrational level in the potential well becomes important.[25] When comparing the lower vibrational level with the upper vibrational level, the upper level has a larger overlap of the wave function and lower gas a small overlap. Since the vibrational level is temperature dependent, it can be seen from this viewpoint that there is a temperature dependence in quantum tunneling as well. However, it is not enough to simply raise the temperature. In the case of vicinity of the zero-point vibration and the high level, the overlap is negligibly small near the zero-point vibration. And it can be seen that the shape of the wave function at the upper level is not suitable for tunneling. In this case, the shape of the potential surface

is different between H and D, so when the distance between the hydrogen donor and acceptor is equal, the overlap of the wave function is different even at the same vibrational level, and the probability of quantum tunneling is different. The isotope effect has also been confirmed when the distance between the acceptor and donor is changed, and the distance at which tunneling is most likely to occur is different for H and D. For example, H is 0.046 nm and D is 0.040 nm. There have been various research examples, but all have concluded that D is shorter.

It is known that in noble metal nanostructures with a particle size of several tens to several hundreds of nm, incident light of a specific wavelength resonates with free electrons in the metal structure, inducing collective oscillations of the free electrons. In particular, it is known that in nanostructures of Au, Ag, Cu, etc., it is possible to adjust the resonant wavelength from the visible to the near-infrared region by controlling the particle size and shape. This phenomenon, called as localized surface plasmon resonance, has two deactivation pathways during decay: radiative and non-radiative deactivation. In the non-radiative deactivation case, the energy of the collective oscillations of electrons is used to generate excitons. It is known that the generation of electron-hole pairs is induced during this relaxation process (Fig. 1.15).[26]

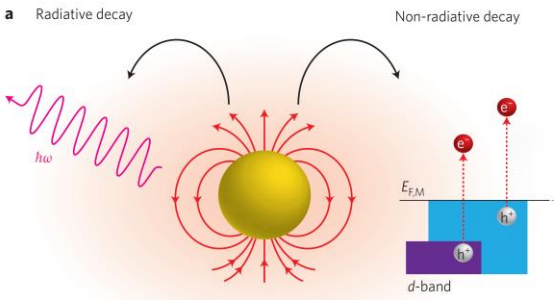

Figure. 1.15. Surface plasmon decay and hot electron-hole generation.

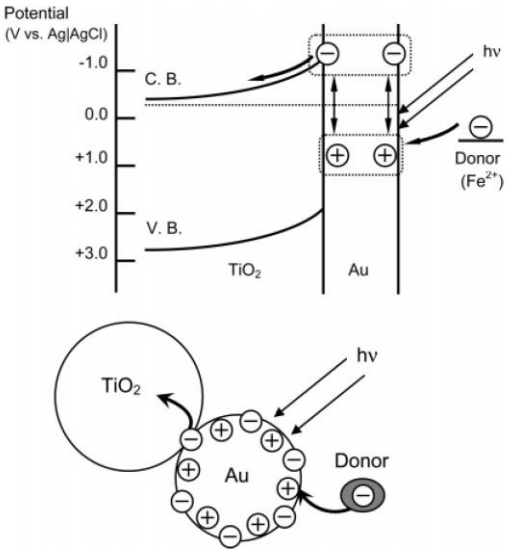

Figure 1.16. schematic image of plasmon induced charge separation and plasmonic photocatalysis.

When a noble metal nanostructure that exhibits plasmon resonance is in contact with an n-type semiconductor, excited electrons generated in the metal, and they are injected into the semiconductor beyond the Schottky barrier of the semiconductor. On the other hand, holes accumulated in the metal due to the electron injection are consumed by oxidation reactions at the semiconductor-metal interface(Fig. 1.16).[27] Research using this system, called a plasmonic photoelectric conversion system, has been progressing, including efforts on water oxidation using near-infrared light.[28] In a system proposed by Moskovits *et al*., Pt, a hydrogen generation catalyst and electron capture agent, was supported on a metal nanostructure to perform water splitting reactions only by light irradiation.[29] Recently, Tatsuma *et al*. have conducted a detailed discussion on charge transfer

efficiency by modulating the mean free path and localization of holes using a structure that exhibits different plasmon modes depending on the direction side of light incident, which is a nanostructure with a large aspect ratio.[30] Meanwhile, Minamimoto has succeeded in determining the absolute electrochemical potential of excitons in the plasmon charge transfer process and visualizing the reaction site by deposition of poly-pyrrole by changing the electrode potential using the polymerization reaction of pyrrole monomers on a plasmon-active substrate.[31] In addition, the reaction proceeds more efficiently with excitons generated in plasmon bound to the surface states at the semiconductor/metal interface.

In 2018, Atwater *et al.* studied a cathode plasmonic electrode that uses excited electrons from a p-type semiconductor for a direct reduction reaction to promote the reduction of CO_2.[32] This research has demonstrated the possibility that plasmonic electrodes can be applied to both oxidation and reduction reactions. However, there is still insufficient research on the specificity of molecular processes at the solid-liquid interface of metal structures and the reaction specificity that depends on solution conditions for these systems.

The plasmonic photocatalyst is a system that uses hot electrons or holes generated in the deactivation process of localized surface plasmons, so in terms of energy, the system converts light energy into electrical energy and then into chemical energy.

On the other hand, an important phenomenon of plasmon-polaritons is the formation of a strong coupling by the interaction with materials. In this strong coupling, when the energy level of the plasmon and the energy level of the material (regardless of vibrational excitation or electronic excitation) are similar, the two levels interact to form a new energy level (Fig. 1.17).[33] The energy level at this time is divided higher and lower than the original level. The higher level is called the upper polariton, and the lower one is called the lower polariton. The importance is that the value becomes different from the original energy level of the material. Theoretically, if a reaction proceeds through the lower polariton, the chemical reaction rate can be modulated. In fact, many optical studies of energy levels in a strong coupling state between plasmon and material have been confirmed. In addition, in a system using a mirrored cavity, which is not a plasmon system, it has been successful in expressing reaction selectivity of the functional groups of organic compounds by forming a strong coupling state between the optical mode of the cavity and the material .

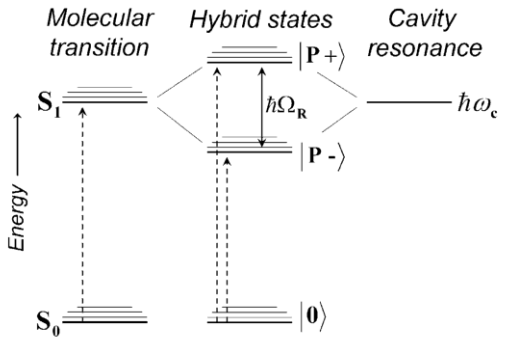

Figure 1.17. Scheme of strong coupling between molecular transition energy and cavity resonance energy.

Furthermore, theoretical predictions suggest that reactions in strong coupling can take new paths through newly created energy levels, making it possible to pass through two reaction paths: one in a non-strongly bound state and one in a strongly bound state (Fig. 1.18).[34, 35]

A system combining plasmonic metals and catalytic metals to reduce formic acid has been reported.[36] This system uses a structure in which Au nanoparticles (AuNPs) with a diameter of about 20 nm are arranged between which Pt nanoparticles with a diameter of about 2 to 3 nm are arranged (Fig. 1.19). In this system, the amount of hydrogen generated did not change with the presence or absence of light in the results for AuNPs alone. In contrast, when PtNPs were present, the amount of hydrogen generated was about twice as much when irradiated with light. As a result of measuring the action spectrum, enhanced electric field, transient absorption, etc. of this system, hydrogen generation activity similar to the absorption spectrum of metal nanostructures was observed, and a strong enhanced electric field was also confirmed between AuNPs and PtNPs. Furthermore, it is noteworthy that the results suggest that there is no electron transfer from Au, which is induced by plasmons by transient absorption, to the catalytic metal Pt. This system shows that plasmon-induced chemical reactions are not simply reactions using plasmon-excited electrons, but that the field generated by plasmons modulates the chemical reaction.

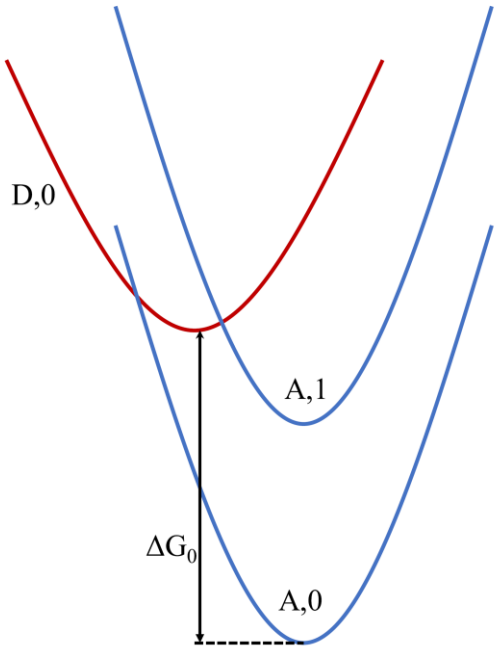

Figure. 1.18. Theoretically expected energy landscape for strong coupling state.

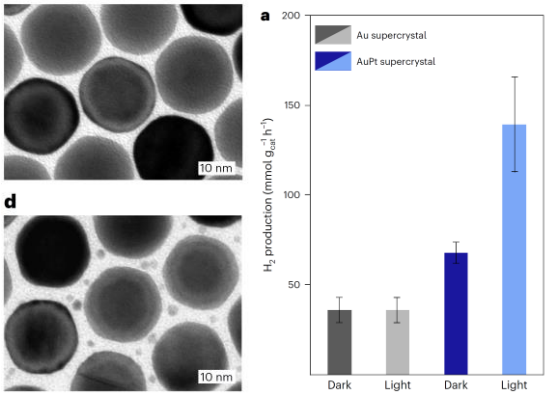

Figure 1.19. SEM image of AuNP and PtNP substrate and activity of these nanoparticle w/ and w/o light.

1.5. Fabrication of nanostructures for the realization of quantum effect

To realize the mentioned substrates in section 1.4, one of the straightforward ways is to fabricate nano sized structures on substrates. Here, it is discussed that two representative methods of fabricating metal nanostructures.

The layout of two-beam interference exposure is shown in Fig. 1.20a.[37] Two laser beams that can

interfere with each other are exposed onto the substrate. In this case, the laser has width, but it is a coherent light. The two lights interfere with each other, and the light strengthens where the phases match, and weakens where the phases do not match. This forms an intensity distribution of interference fringes on the resist surface as shown in the following equations.

$$I(x) = (I_1 + I_2)[1 + 2\sqrt{I_1 I_2} \times \cos\left(\frac{2\pi x}{P}\right)]\frac{\sin(\Delta\phi/2)}{\Delta\phi/2} \quad (18)$$

$$P = \frac{\lambda}{2n\sin\theta} \quad (19)$$

I_1 and I_2 are the intensities of the incident light, P is the period of the interference fringes, n is the refractive index of the space through which the light propagates (usually in air, so $n = 1$), λ is the wavelength of the light, θ is the angle of incidence of the light, and ϕ is the term for the phase of the interference fringes, and if the interference screen does not change during exposure, $\Delta\phi = 0$. In other words, the pitch width can be changed by adjusting the angle of incident light. Also, as can be seen from the pitch width formula, the resolution limit of exposure is $\lambda/2n$.

If there is reflection between the resist and the substrate, this reflected light can also cause interference, and for substrates with high reflectivity, an anti-reflection layer may be placed to reduce the effects of reflection. Fig. 1.20b shows a schematic diagram of the interference exposure equipment. With this equipment, the angle of incident light can be changed by adjusting the angle of the mirror above the substrate. Electron beam lithography

(a)

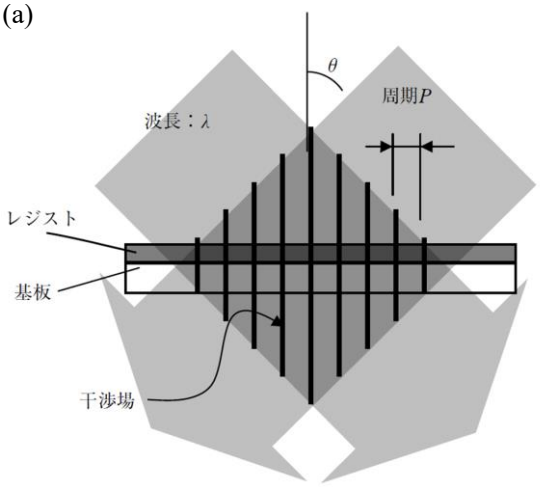

(b)

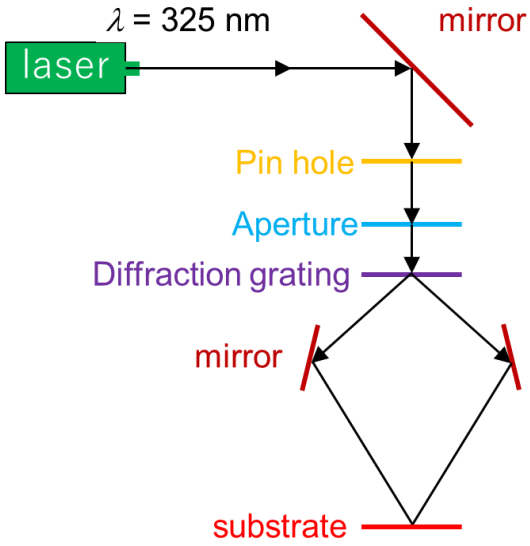

(a) (b)

Figure 1.20. (a)The state of light near a surface during interference exposure, (b) schematic image of utilized interference exposure system.

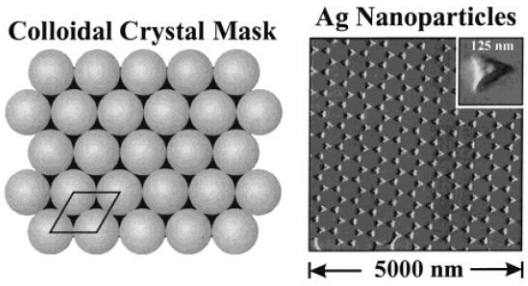

Figure 1.21. (a) Beads orientation on surface of NSL method, after this one can fabricate structures using EB deposition or spatter and so on, (b) AFM image for NSL method nanostructures.

(EBL) is one of the useful methods to form fine resist patterns. In contrast of (EBL), interference exposure has the advantages of being able to expose a large area all at once and using a simple exposure system.

In addition to interference exposure, there is also a template method called nanosphere lithography (NSL).[38] In this method, beads with uniform size are arranged on a substrate in a two-dimensional closest-packed manner. As a result, gaps are created between the beads (Fig. 1.21a). By deposition of metal on the substrate by sputtering or other methods and removing the beads, it is possible to fabricate a periodic nanostructure (Fig. 1.21b).

1.6 Purpose in this study

It is possible to modulate the reactivity of plasmon coupling chemical reactions utilizing metal nanostructures. However, there are few examples that applying nanostructures substrate to electrochemical systems, especially HER which is thought as an archetype of electrochemistry. Doing experiments and resulting from this, it is possible to discuss the reactivity modulation of HER by quantum effect utilizing nanostructures. The purpose of this study is to investigate what properties of metal nanostructures (metal species, size, mode volume, coherence, localized electric field) modulate the reactivity of chemical reactions and what kinetic parameters (concentration, activation energy, binding energy, etc.) accelerate chemical reaction rates by metal nanostructures, how modified reaction molecular mechanism by modulating kinetic parameters.

In Chapter 2, I investigated the activity of HER using localized surface plasmon resonance by metal nanostructures in the mm range on a p-type semiconductor, depending on the solution pH, and confirmed the reactivity modulation due to the interaction between plasmon polaritons and the material system. This revealed that it is possible to modulate reactivity and demonstrated the controlling electron transfer reactions using polaritons.

In Chapter 3, in order to compare the activity of various types of metal nanostructures, I developed a method to calculate the current value from HER bubbles on the electrode surface. The bubble observation on the electrode surface was recorded as a video synchronized with a potential and the bubble formation and growth were obtained. The current value at the observation site was calculated from the bubble growth rate. The validity of this method was also discussed by comparing the current value calculated from the bubbles with the results of classical electrochemical measurements and the actual current, and it was confirmed that this method can measuring the local current of the electrode.

In Chapter 4, I fabricated various metal nanostructures on a glassy carbon electrode, and by applying potential, I simultaneously performed HER on multiple types of metal nanostructures to investigate their activity in a screening. For this activity investigation, I used the method in Chapter 3 to calculate the current value from bubbles. The polariton mode of each metal nanostructure was discussed using the finite-difference time-domain method. By closely examining the activity and

polariton mode of each metal nanostructure, I found the possibility of activity modulation depending on the polariton mode. Furthermore, I found the possibility of elementary process modulation as a result of the emergence of a new reaction pathway due to quantum effects. I guessed that this is due to the modulation of electron transfer reactions at the electrode interface and the special environment of the material system around the electrode surface. This revealed that it is possible to control the reactivity by controlling the metal nanostructure without changing the electrode material. Furthermore, by fabricating a highly active metal nanostructure over a large area and performing electrochemical measurements, I demonstrated that it is more active than a normal metal electrode.

Through these experiments, I have demonstrated the reactivity different from that of ordinary electrode materials in HER using localized surface plasmon resonance. To discuss the polariton mode dependence of the reactivity modulation, I developed the method to indirectly obtain HER activity by observing HER bubbles. Using this method, I proceeded with HER in metal nanostructures, each of which had a different plasmon mode, and by comparing the activity in a screening manner, I found that the reaction was highly active in a specific plasmon mode. Furthermore, I found that the influence of this polariton may affect not only the electrode interface but also the materials in its vicinity.

In conclusion, this doctoral thesis proves that polariton states could be applied to control electron transfer reactions, and I proposed a guideline for controlling the reactivity of chemical reactions by introducing quantum effects, particularly strong coupling. As a result, it enabled to control the reactivity of specific elementary steps in multi-electron transfer reactions, which are difficult to control with normal approach to design electrode catalysis, thus breaking through the limitations of electrocatalytic chemistry.

1.7 References

1. Sahin, M. E. An Overview of Different Water Electrolyzer Types for Hydrogen Production. **17**, 4944 (2024).
2. McCrory, C. C. L. *et al.* Benchmarking Hydrogen Evolving Reaction and Oxygen Evolving Reaction Electrocatalysts for Solar Water Splitting Devices. *J. Am. Chem. Soc.* **137**, 4347–4357 (2015).
3. Nishiyama, H. *et al.* Photocatalytic solar hydrogen production from water on a 100-m^2 scale. *Nature* **598**, 304–307 (2021).
4. Miseki, Y., Tamano, M., Watanabe, K. & Sayama, K. Demonstration of Scalable Water Splitting into H2 and O2 by a Flow-Type Photocatalysis-Electrolysis Hybrid System Using a Highly Stable Photocatalyst. *ACS Appl. Mater. Interfaces* **16**, 60219–60230 (2024).
5. Stoerzinger, K. A., Qiao, L., Biegalski, M. D. & Shao-Horn, Y. Orientation-dependent oxygen evolution activities of rutile IrO_2 and RuO_2. *J. Phys. Chem. Lett.* **5**, 1636–1641 (2014).
6. Montoya, J. H. *et al.* Materials for solar fuels and chemicals. *Nat. Mater.* **16**, 70–81 (2016).
7. Gao, R. *et al.* Structural Variations of Metal Oxide-Based Electrocatalysts for Oxygen Evolution Reaction. *Small Methods* **5**, 1–38 (2021).
8. Yoo, J. S., Rong, X., Liu, Y. & Kolpak, A. M. Role of Lattice Oxygen Participation in Understanding Trends in the Oxygen Evolution Reaction on Perovskites. *ACS Catal.* **8**, 4628–4636 (2018).
9. Tafel, J. About the polarization during cathodic hydrogen evolution. *Z. phys. Chem* vol. 50 641 (1905).
10. Shinagawa, T., Garcia-Esparza, A. T. & Takanabe, K. Insight on Tafel slopes from a microkinetic analysis of aqueous electrocatalysis for energy conversion. *Sci. Rep.* **5**, 1–21 (2015).
11. Østergaard, F. C., Bagger, A. & Rossmeisl, J. Predicting catalytic activity in hydrogen evolution reaction. *Curr. Opin. Electrochem.* **35**, 101037 (2022).
12. Strmcnik, D. *et al.* Improving the hydrogen oxidation reaction rate by promotion of hydroxyl adsorption. *Nat. Chem.* **5**, 300–306 (2013).
13. Danilovic, N., Subbaraman, R., Strmcnik, D., Stamenkovic, V. R. & Markovic, N. M. Electrocatalysis of the HER in acid and alkaline media. *J. Serbian Chem. Soc.* **78**, 2007–2015 (2013).
14. Subbaraman, R. *et al.* Trends in activity for the water electrolyser reactions on 3d M(Ni,Co,Fe,Mn) hydr(oxy)oxide catalysts. *Nat. Mater.* **11**, 550–557 (2012).
15. Ledezma-Yanez, I. *et al.* Interfacial water reorganization as a pH-dependent descriptor of the hydrogen evolution rate on platinum electrodes. *Nat. Energy* **2**, 1–24 (2017).
16. Monteiro, M. C. O., Goyal, A., Moerland, P. & Koper, M. T. M. Understanding Cation Trends

for Hydrogen Evolution on Platinum and Gold Electrodes in Alkaline Media. *ACS Catal.* **11**, 14328–14335 (2021).

17. Monteiro, M. C. O., Dattila, F., López, N. & Koper, M. T. M. The Role of Cation Acidity on the Competition between Hydrogen Evolution and CO_2 Reduction on Gold Electrodes. *J. Am. Chem. Soc.* **144**, 1589–1602 (2022).
18. Bender, J. T. *et al.* Understanding Cation Effects on the Hydrogen Evolution Reaction. *ACS Energy Lett.* **8**, 657–665 (2023).
19. Quaino, P., Juarez, F., Santos, E. & Schmickler, W. Volcano plots in hydrogen electrocatalysis-uses and abuses. *Beilstein J. Nanotechnol.* **5**, 846–854 (2014).
20. Wiberg, K. B. The Deuterium Isotope Effect. *Chem. Rev.* **55**, 713–743 (1955).
21. Bockris, J. O. & Srinivasan, S. Theoretical Calculations of the Separation Factors in the Hydrogen Evolution Reaction for the Slow Recombination Mechanism. *J. Electrochem. Soc.* **111**, 858 (1964).
22. Enyo, M. Change of mechanism of the hydrogen electrode reaction with overpotential-III. Potential dependence of the deuterium separation factor on Pt, Au and Ni cathodes. *Electrochim. Acta* **21**, 15–20 (1976).
23. Minamimoto, H., Osaka, R. & Murakoshi, K. In-situ observation of isotopic hydrogen evolution reactions using electrochemical mass spectroscopy to evaluate surface morphological effect. *Electrochim. Acta* **304**, 87–93 (2019).
24. Krishtalik, L. I. The mechanism of the proton transfer: an outline. *Biochim. Biophys. Acta - Bioenerg.* **1458**, 6–27 (2000).
25. Parkin, G. Temperature-Dependent Transitions Between Normal and Inverse Isotope Effects Pertaining to the Interaction of H−H and C−H Bonds with Transition Metal Centers. *Acc. Chem. Res.* **42**, 315–325 (2009).
26. Clavero, C. Plasmon-induced hot-electron generation at nanoparticle/metal-oxide interfaces for photovoltaic and photocatalytic devices. *Nat. Photonics* **8**, 95–103 (2014).
27. Tian, Y. & Tatsuma, T. Mechanisms and applications of plasmon-induced charge separation at TiO2 films loaded with gold nanoparticles. *J. Am. Chem. Soc.* **127**, 7632–7637 (2005).
28. Nishijima, Y. *et al.* Near-Infrared Plasmon-Assisted Water Oxidation. *J. Phys. Chem. Lett.* **3**, 1248–1252 (2012).
29. Mubeen, S. *et al.* An autonomous photosynthetic device in which all charge carriers derive from surface plasmons. *Nat. Nanotechnol.* **8**, 247–251 (2013).
30. Nishi, H., Sakamoto, M. & Tatsuma, T. Local trapping of energetic holes at gold nanoparticles on TiO_2. *Chem. Commun.* **54**, 11741–11744 (2018).
31. Minamimoto, H. *et al.* Visualization of Active Sites for Plasmon-Induced Electron Transfer Reactions Using Photoelectrochemical Polymerization of Pyrrole. *J. Phys. Chem. C* **120**, 16051–

16058 (2016).

32. Duchene, J. S., Tagliabue, G., Welch, A. J., Cheng, W. H. & Atwater, H. A. Hot Hole Collection and Photoelectrochemical CO_2 Reduction with Plasmonic Au/p-GaN Photocathodes. *Nano Lett.* **18**, 2545–2550 (2018).
33. Hutchison, J. A., Schwartz, T., Genet, C., Devaux, E. & Ebbesen, T. W. Modifying Chemical Landscapes by Coupling to Vacuum Fields. *Angew. Chemie Int. Ed.* **51**, 1592–1596 (2012).
34. Semenov, A. & Nitzan, A. Electron transfer in confined electromagnetic fields. *J. Chem. Phys.* **150**, 174122 (2019).
35. Hayashi, T., Fukushima, T. & Murakoshi, K. Role of cavity strong coupling on single electron transfer reaction rate at electrode–electrolyte interface. *J. Chem. Phys.* **161**, (2024).
36. Herran, M. *et al.* Plasmonic bimetallic two-dimensional supercrystals for H_2 generation. *Nat. Catal.* **6**, 1205–1214 (2023).
37. Amako, J. & Sawaki, D. Deep-UV レーザーを用いたサブ波長構造の創製-干渉露光法によるレジストパターニング-. 精密工学会誌 **74**, (2008).
38. Haynes, C. L. & Van Duyne, R. P. Nanosphere lithography: A versatile nanofabrication tool for studies of size-dependent nanoparticle optics. *J. Phys. Chem. B* **105**, 5599–5611 (2001).

2 Plasmon Induced Hydrogen Evolution Reaction

2.1 Introduction

The efficient use of the light energy is still a big challenge for the realization of the sustainable society. From this point of view, photo-induced chemical reactions using semiconductor electrode could be regarded as the promising approaches for the photo-energy storage. Until now, various photocatalytic systems using the wide-band gap semiconductors have been established. However, its wide band gap energy often limits the efficiency because the visible light cannot be used for chemical reactions.[1,2] As the breakthrough for it, several systems, such as the dye synthesized solar cell or perovskite solar cell, has been proposed for improving the photo-response ability in the visible wavelength region.[3,4] In addition to them, recently, the usage of the metal nanostructures which lead to the excitation of the localized surface plasmon resonance (LSPR) has been received much attention.[5,6] By supporting the plasmonic structure, the visible light response ability is added to the system beyond the limitation of the band gap energy of semiconductor electrodes.[7,8] Previously reported various type of the plasmonic photoconversion system is mainly composed of the n-type semiconductor electrode with the plasmonic metal nanostructures. Several types of the mechanism for the chemical reactions, such as plasmon-induced resonance energy transfer or plasmon-induced metal-to-semiconductor interfacial charge transfer transition, have been suggested.[9,10] One of well accepted mechanism is that the electrons excited in the metal structures were injected into the conduction band of n-type semiconductor and the remained holes are consumed through the oxidation reaction at the metal-semiconductor interface.[8,11] As to this plasmon-induced charge transfer process, various type examinations have been attempted to understand the detail reaction process.[12] In previous study, I have not only visualized the reaction active sites but also determined the absolute electrochemical potential of the reaction active species by the introduction of the polymerization reaction of the conductive polymer.[13] The point for it is that the excited holes generates at much positive than the Fermi level of the metal nano-particles, and are trapped at the metal-semiconductor interface for the efficient multi-electron reactions.

Regarding to the reduction reaction on the plasmonic catalyst, various types of demonstration have been reported.[14,15] Among them, the prevail system is to control the reduction reaction on the counter electrode as the side reaction of the oxidation reaction at metal semiconductor interface by introducing the noble metal. Up to date, the high efficient water splitting reaction or the ammonium synthesis have been achieved using this system. [16,17] On the other hand, very recently, the combination of the p-type semiconductor electrode with the plasmonic Au nanoparticle have been proposed as the plasmonic cathode.[18,19] The plasmonic cathode system shows the high selectivity for CO_2 reduction reaction through the efficient accumulation of excited electrons at the metal surface. From such backgrounds, although various attempts have been carried out, the systems need further investigations for the discussion about the detail molecular process and the charge transfer

mechanism to clarify the characteristics of the plasmonic cathode systems.

Based on above backgrounds, I have attempted to establish the visible light-induced hydrogen evolution system by the introduction of the plasmonic structure onto the surface of the p-type semiconductor electrode. Because it is known that unique molecular process or the intermediate state appear at the plasmonic surface, the detail investigation of the reactivity of the system should be important. In this study, photochemical measurements adopting distinct pH conditions have been conducted and, as the results, I have confirmed the unique characteristics of the pH dependence on the plasmonic cathodic reaction.

2.2 Experiments

At the present experiments, the single crystal p-type gallium phosphide ((111), Zn-doped: 4.8×10^{18} cm^{-3}) (p-GaP) was purchased from E&M Corporation ltd. and used as the photo-cathode electrode. Plasmonic nanostructures were prepared by the nano-sphere lithography method.[20] The diameter of the polystyrene bead used as the template was 350 nm. Prepared structures were examined through the atomic force microscopy (AFM) measurements. The photocurrent measurements have been performed using the three-electrode cell. The plasmonic p-GaP electrode, Pt plate, and Ag/AgCl electrode were used as the working, counter, and reference electrodes, respectively. For the photocurrent measurements, the electrode potential was set to −0.6 V vs. Ag/AgCl. The plasmonic p-GaP electrode was contacted to a stainless plate with an In-Ga ohmic contact. The photocurrent measurements were performed with Xe lamp for the illumination of the light wavelength in 550-900 nm region.

2.3 Results and discussion

First of all, I have defined the photocurrent density as $i_{Ag/GaP}$ as indicated in Fig. 2.1. The $i_{Ag/GaP}$ values were corresponding to the difference between the photocurrents obtained at the initial and end of light illumination.

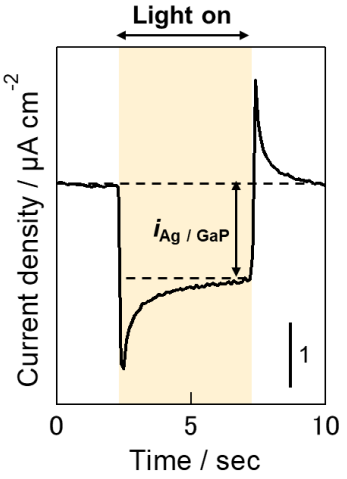

Figure 2.1. | Photocurrent measurements using plasmonic p-GaP electrodes under neutral condition. The electrolyte solutions was 0.5 M Na_2SO_4aq. The electrode potential was kept at −0.6 V. The incident wavelength was $\lambda > 550$ nm.

Fig. 2.2a and b show the AFM image of Ag dimer structures and the polarized extinction spectra of it, respectively. From AFM measurements, I have confirmed the successful preparation of the uniform well-defined Ag dimer structures on the entirely surface of p-GaP electrode. Extinction spectra obtained with the incident parallelly and vertically polarized to the long axis of the dimer (Fig. 2.2c). With the polarized direction parallel to the long axis direction, the Ag dimer structures show the absorption in the visible to near infrared region. The resonance peak is derived from the dipole-dipole interaction between the Ag nanostructures.[21] This optical character is good agreement with the results in previous report.[22] As shown in the left panel of Fig. 2.2d, by using this electrode and p-GaP without Ag dimer structures, I have carried out the photocurrent measurements in the neutral solution under visible light illumination (λ > 550 nm). Due to the wide band gap of p-GaP (E_g = 2.3 eV (λ = 540 nm)),[23] the p-GaP electrode did not show the photocurrent response against the visible light illumination with the photon energy of less than 1.9 eV. Slight increment of the photocurrents would be originated from the surface state of GaP. In addition, I have examined the stability of the system by the multi time light illuminations and confirmed the stable light current

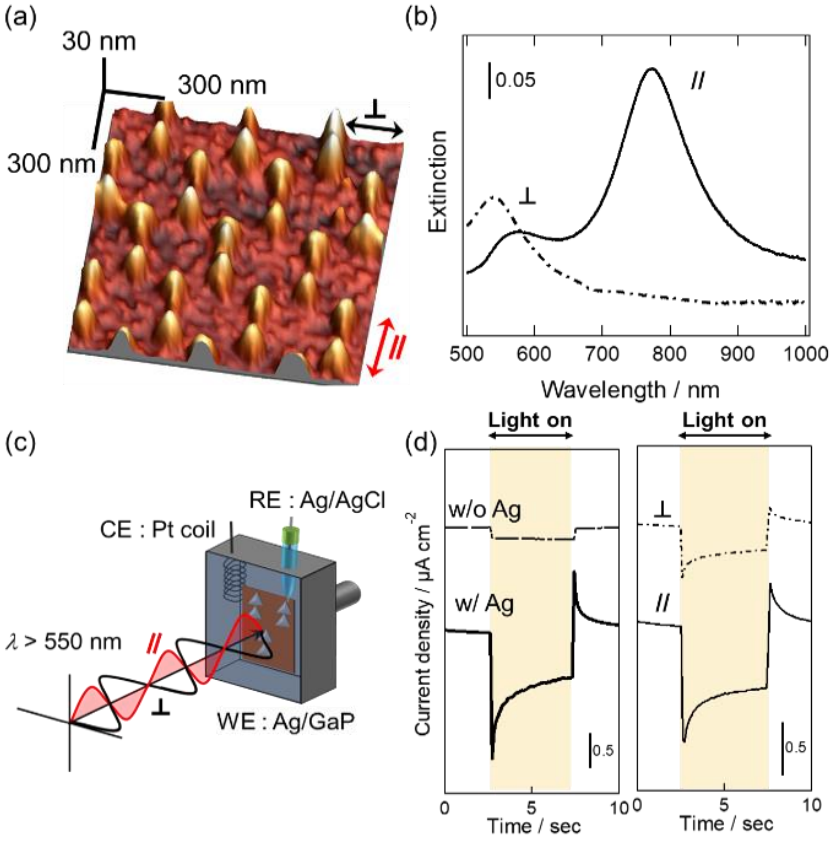

Figure. 2.2. (a) 3D AFM image of prepared Ag nanostructures. (b) Polarized extinction spectra of Ag dimer structures on glass substrate. The polarized directions were parallel (solid) and vertical (broken) to the long axis of Ag dimer structures. (c) Schematic illustration of the three-electrode photoelectrochemical cell. (d) Photocurrents of p-GaP electrodes without/with Ag dimer structures (left). Photocurrents on the p-GaP with Ag dimer structures under the visible light illumination (550 < λ < 900 nm) polarized to parallel (solid) and vertical (broken) direction (right). The electrode potential was kept at −0.6 V in an aqueous electrolyte solution of 0.5 M Na_2SO_4 (neutral).

generations. At the present experiment, the Ag structures were kept at the negative potential. Thus, the surface would be prevented from the oxidation or dissolution reactions.

On the contrary, in the case for the plasmonic photoconversion electrode, the photocurrent generation was clearly observed under the visible light illumination (left panel of Fig. 2.2d). In addition, I have also observed the dependence of the light polarization dependence on the photocurrent. The parallelly polarized incident light to the long axis of the Ag dimer structures results in the two times higher photocurrent than that obtained at the vertically polarized light illumination. This result reflects the optical property of the plasmonic Ag-dimers as shown in Fig. 2.2b. Based on these results, observed photocurrent is attributed to the plasmon-induced hydrogen evolution system by visible light illumination on p-GaP. Regarding to the reaction mechanism of it, in this system, the hydrogen evolution reaction is triggered by the excited electrons in the metal nanostructures while the generated holes were injected into the valence band of the p-GaP. The flat band potential of p-GaP is located at 0.3 V vs. Ag/AgCl at pH = 7.[24] Thus, considering the energy of incident photons from 1.4 eV to 2.3 eV (550 nm < λ < 900 nm), plasmonically excited electrons with estimated minimum electrochemical potentials from −1.1 V to −2.0 V vs. Ag/AgCl could contribute to the hydrogen evolution reactions in the present system.

To discuss about the characteristics to the plasmonic cathode system, I have investigated the pH dependence on the hydrogen evolution reaction. Fig. 2.3a shows the results of the photocurrent density ($i_{Ag/GaP}$) using plasmonic p-GaP electrodes with Ag dimer structures under different pH conditions. The solution conditions were defined as acid, neutral, and base. It should be noteworthy that $i_{Ag/GaP}$ show highest values at neutral condition than those at acid and base. Fig. 2.3b shows the not only $i_{Ag/GaP}$ values, but also the photocurrent density of p-GaP without Ag dimer structures (i_{GaP}) obtained in the same electrolytes under band gap excitation condition (λ > 380 nm illumination) for the comparison. As can be seen in figures, the photocurrent values were different from that in Fig. 2.2. As reported in previous report, the photocurrent density for the plasmonic system is sensitively affected by the surface defect sites of semiconductor substrate.[25] Thus, this could be derived from not only for the inhomogeneous plasmonic structures but also the surface state of p-GaP. I have confirmed that the difference depending on the electrode was within the range of about 2 times at maximum. Obviously, the i_{GaP} value in the acidic solution is highest while the basic condition shows lowest one. Generally, the hydrogen evolution reaction under the acidic condition shows kinetically higher rate compared to those under neutral or basic condition, because the hydrogen evolution is the proton-coupled process.[26] The redox potentials of hydrogen are at around −0.3 and −0.9 V. vs. Ag/AgCl under acidic and basic condition, respectively. Therefore, observed pH dependence of i_{GaP} is quite reasonable both in the kinetics and the thermodynamics point of views. In spite of these principles, as indicated in Fig. 2.3, the observed $i_{Ag/GaP}$ obtained in the neutral solution was larger

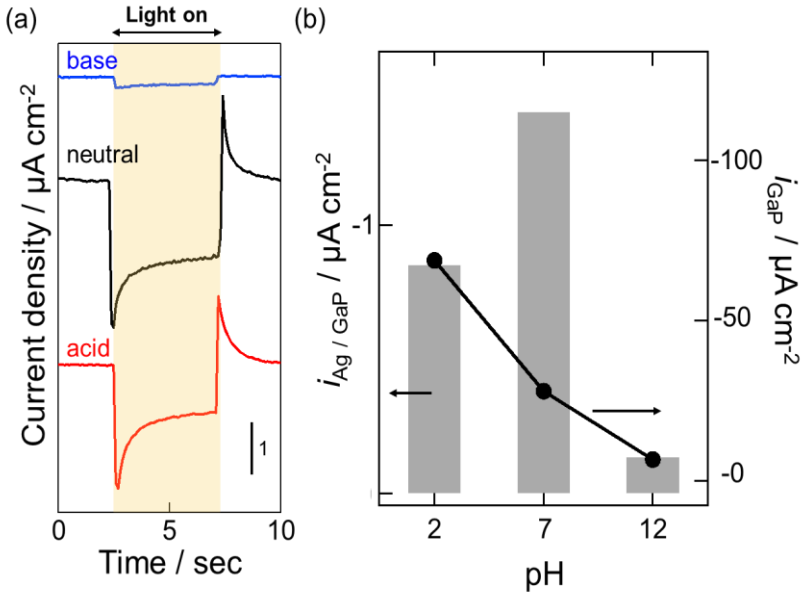

Figure 2.3. (a) Photocurrent measurements using plasmonic p-GaP electrodes under different pH conditions. The electrolyte solutions were 0.01 M NaOH with 0.5 M Na_2SO_4aq. (base), 0.5 M Na_2SO_4aq. (neutral), and 0.05 M H_2SO_4 with 0.5 M Na_2SO_4aq. (acid). The electrode potential was kept at −0.6 V. (b) The $i_{Ag/GaP}$ and i_{GaP} values obtained at respective pH values. The illuminated light wavelength for the $i_{Ag/GaP}$ and i_{GaP} measurements were $\lambda >$ 550 nm and $\lambda >$ 380nm, respectively.

than that in the acidic. This would imply that the visible light induced plasmonic hydrogen evolution reactions proceed via the unique surface molecular process, especially under the neutral condition.

It is well known that the hydrogen evolution reactions proceed via multiple surface molecular processes including three steps; (20) Volmer, (21) Tafel, and (22) Heyrovsky reactions.[26]

$$H^+ + e^- \rightarrow H_{ad} \qquad (20)$$

$$H_{ad} + H_{ad} \rightarrow H_2 \qquad (21)$$

$$H_{ad} + H^+ + e^- \rightarrow H_2 \qquad (22)$$

The initial step which forms the adsorbed hydrogens (Volmer step) depends on the metal species, surface morphology, or the crystal plane of the surface while the Tafel and Heyrovsky are determined by the hydrogen coverage.[27] In the acidic solution, due to the relatively faster process of the Volmer process, the kinetics for it is generally faster than that under other condition. It has been reported that the rate constant of the Volmer step in the acidic media is at least ten times faster than that under the basic condition.[28,29] Considering the fact that the photocurrents value in the neutral solution was higher than that under the acidic condition, it can be expected that, at the surface of the plasmonic Ag structures, the surface process, such as the Volmer or Tafel process, would be accelerated by the plasmonic field. In recent previous study, it has been reported that the characteristics intermediate as the consequence of the reaction acceleration at Au nanostructures on n-type TiO_2 electrode, resulting in the improvement in the water oxidation, appears especially under the neutral condition.[30] Therefore, the results in Fig. 2.3 would imply that the similar effect for the decrease of the overpotential specifically express on the plasmonic cathode system. As the future work of this study, I am going to examine the kinetic isotope effect on the reaction to probe the detailed surface

molecular processes. Consequently, it can be said that this finding is useful information for the design of the further efficient plasmonic photoconversion devices.

2.4 Conclusions

In summary, by the combination of the p-GaP and Ag dimer structures, visible light induced hydrogen evolution reaction system has been successfully achieved. The photocurrent generations depending on the polarized direction of the incident light were observed, resulting in the excitation of the LSPR. Through the electrochemical photocurrent measurements under different pH conditions, I have confirmed the improved reactivity of the reaction, especially under the neutral condition. This fact proves the unique molecular process triggered by LSPR. I am sure that the insight proposed through current experiments would open the further possibility for the future plasmonic cathodic system.

2.5 Reference

1. Hoffmann, M. R., Martin, S. T., Choi, W. & Bahnemann, D. W. Environmental Applications of Semiconductor Photocatalysis. *Chem. Rev.* **95**, 69–96 (1995).
2. Andrew Mills, S. L. H. An overview of semiconductor photocatalysis. *J. Photochem. Photobiol. A Chem.* **108**, 1–35 (1997).
3. O'Regan, B. & Grätzel, M. A low-cost, high-efficiency solar cell based on dye-sensitized colloidal TiO_2 films. *Nature* **353**, 737–740 (1991).
4. Kojima, A., Teshima, K., Shirai, Y. & Miyasaka, T. Organometal halide perovskites as visible-light sensitizers for photovoltaic cells. *J. Am. Chem. Soc.* **131**, 6050–6051 (2009).
5. Brongersma, M. L., Halas, N. J. & Nordlander, P. Plasmon-induced hot carrier science and technology. *Nat. Nanotechnol.* **10**, 25–34 (2015).
6. Minamimoto, H., Oikawa, S., Li, X. & Murakoshi, K. Plasmonic Fields Focused to Molecular Size. *ChemNanoMat* **3**, 843–856 (2017).
7. Zhao, G., Kozuka, H. & Yoko, T. Sol-gel preparation and photoelectrochemical properties of TiO2 films containing Au and Ag metal particles. *Thin Solid Films* **277**, 147–154 (1996).
8. Tian, Y. & Tatsuma, T. Mechanisms and Applications of Plasmon-Induced Charge Separation at TiO 2 Films Loaded with Gold Nanoparticles. *J. Am. Chem. Soc.* **127**, 7632–7637 (2005).
9. Li, J. *et al.* Plasmon-induced resonance energy transfer for solar energy conversion. *Nat. Photonics* **9**, 601–607 (2015).
10. Wu, K., Chen, J., Mcbride, J. R. & Lian, T. Efficient hot-electron transfer by a plasmon-induced interfacial charge-transfer transition. **349**, 632–635 (2015).
11. Nishijima, Y., Ueno, K., Yokota, Y., Murakoshi, K. & Misawa, H. Plasmon-assisted photocurrent generation from visible to near-infrared wavelength using a Au-nanorods/TiO_2 electrode. *J. Phys.*

Chem. Lett. **1**, 2031–2036 (2010).

12. Kazuma, E. & Tatsuma, T. Photoinduced reversible changes in morphology of plasmonic Ag nanorods on TiO_2 and application to versatile photochromism. *Chem. Commun.* **48**, 1733–1735 (2012).
13. Minamimoto, H. *et al.* Visualization of Active Sites for Plasmon-Induced Electron Transfer Reactions Using Photoelectrochemical Polymerization of Pyrrole. *J. Phys. Chem. C* **120**, 16051–16058 (2016).
14. Linic, S., Christopher, P. & Ingram, D. B. Plasmonic-metal nanostructures for efficient conversion of solar to chemical energy. *Nat. Mater.* **10**, 911–921 (2011).
15. Wang, P., Huang, B., Dai, Y. & Whangbo, M. H. Plasmonic photocatalysts: Harvesting visible light with noble metal nanoparticles. *Phys. Chem. Chem. Phys.* **14**, 9813–9825 (2012).
16. Mubeen, S. *et al.* An autonomous photosynthetic device in which all charge carriers derive from surface plasmons. *Nat. Nanotechnol.* **8**, 247–251 (2013).
17. Oshikiri, T., Ueno, K. & Misawa, H. Plasmon-induced ammonia synthesis through nitrogen photofixation with visible light irradiation. *Angew. Chemie - Int. Ed.* **53**, 9802–9805 (2014).
18. Duchene, J. S., Tagliabue, G., Welch, A. J., Cheng, W. H. & Atwater, H. A. Hot Hole Collection and Photoelectrochemical CO_2 Reduction with Plasmonic Au/p-GaN Photocathodes. *Nano Lett.* **18**, 2545–2550 (2018).
19. Duchene, J. S. *et al.* Optical Excitation of a Nanoparticle Cu/p-NiO Photocathode Improves Reaction Selectivity for CO_2 Reduction in Aqueous Electrolytes. *Nano Lett.* **20**, 2348–2358 (2020).
20. Sawai, Y., Takimoto, B., Nabika, H., Ajito, K. & Murakoshi, K. Observation of a small number of molecules at a metal nanogap arrayed on a solid surface using surface-enhanced Raman scattering. *J. Am. Chem. Soc.* **129**, 1658–62 (2007).
21. Atay, T., Song, J. & Nurmikko, A. V. Strongly Interacting Plasmon Nanoparticle Pairs: From Dipole−Dipole Interaction to Conductively Coupled Regime. *Nano Lett.* **4**, 1627–1631 (2004).
22. Nagasawa, F., Takase, M. & Murakoshi, K. Raman enhancement via polariton states produced by strong coupling between a localized surface plasmon and dye excitons at metal nanogaps. *J. Phys. Chem. Lett.* **5**, 14–19 (2014).
23. Butler, M. A. & Ginley, D. S. P-Type GaP as a Semiconducting Photoelectrode. *J. Electrochem. Soc.* **127**, 1273–1278 (1980).
24. Horowitz, G. Flatband potential of a p -type phosphide electrode. *J. Appl. Phys.* **49**, 3571–3573 (1978).
25. Minamimoto, H. *et al.* Potential energy shift of the Fermi level at plasmonic structures for light-energy conversion determined by graphene-based Raman measurements. *J. Chem. Phys.* **152**, 124702 (2020).

26. Bockris, J. O. O. Recent Developments in the Study of Hydrogen Overpotential. *Chem. Rev.* **43**, 525–577 (1948).
27. Ruderman, A. *et al.* Current transients for the hydrogen evolution reaction at high overpotentials on silver electrodes in acid solutions: Experiments and modelling. *Electrochim. Acta* **109**, 403–410 (2013).
28. Bai, L., Harrington, D. A. & Conway, B. E. Behavior of overpotential—deposited species in Faradaic reactions—II. ac Impedance measurements on H2 evolution kinetics at activated and unactivated Pt cathodes. *Electrochim. Acta* **32**, 1713–1731 (1987).
29. Barber, J., Morin, S. & Conway, B. E. Specificity of the kinetics of H_2 evolution to the structure of single-crystal Pt surfaces, and the relation between opd and upd H. *J. Electroanal. Chem.* **446**, 125–138 (1998).
30. Suzuki, K., Li, X., Wang, Y., Nagasawa, F. & Murakoshi, K. Active Intermediates in Plasmon-Induced Water Oxidation at Au Nanodimer Structures on a Single Crystal of TiO_2. *ACS Energy Lett.* **5**, 1252–1259 (2020).

3 Bubbles Observation for Evaluation of Hydrogen Evolution Reaction Activity

3.1 Introduction

HER is the important reaction for next green energy society.[1-4] The HER activities are routinely investigated by relationship between current density and electrochemical potential. [5-11] However, it is still challenging to investigate the high current density region. [12-15] In case with the high current density region, evaluation of electrochemical activity can be problematic due to the bubble formation at the electrode. [16,17] These bubble formation can be related to the nucleation and growth of the bubbles. Takanabe *et al*. reported the use of the electrolyte engineering for the attenuation of the bubble formation.[18] Koper et al. reported the use of the bubble with the relation to the Hoffmeister effect in intermolecular interaction of electrolyte solution.[19] Therefore, there is still difficulty for the understanding of the bubble formation process from the electrode–electrolyte interface.

Here, I would like to propose that the utilization of the bubbles growth as descriptor of the electrocatalytic activity. Ag was selected as the nominal electrodes in the HER experiments.[20-23] Hydrogen bubble evolution behavior was evaluated from electrochemical measurements and the video observation under electrochemical potential control. The growth processes were monitored by image-analysis as the descriptor for the HER. I discuss the utilization of the bubble growth process as a descriptor of the electrocatalytic activity.

3.2 Experiment

The video camera was set above the working electrode for the bubble observation (Fig. 3.1a). The telecentric lens, TPC6-MS65D, was utilized as the objective lens for observation of the bubbles without the defocusing based on the orthographic view of the bubbles from the Ag working electrode. Electrochemical cell with hydrostatic pressure component, obtained from the Syn corporation Ltd., Japan, was utilized for the evaluation of pressure dependent HER behavior. Electrochemical cell vessel was introduced in the high-pressure chamber inside the electrochemical cell (Fig. 3.1b). Due to the high hydrostatic pressure application in the experimental cell, I avoided to use conventional reference electrode such as the Ag | AgCl | KCl with glass jacket or glass flits components. Therefore, I used a Au wire as a quasi-reference electrode. The electrochemical potential for the quasi-reference electrode was calibrated based on the onset potential of the HER in the same electrolyte condition. Hereafter, all the electrochemical potential was referenced to the reversible hydrogen electrode (RHE). In order to investigate the water electrolysis at neutral condition, I utilized the 0.25 M Na_2SO_4 as electrolyte.

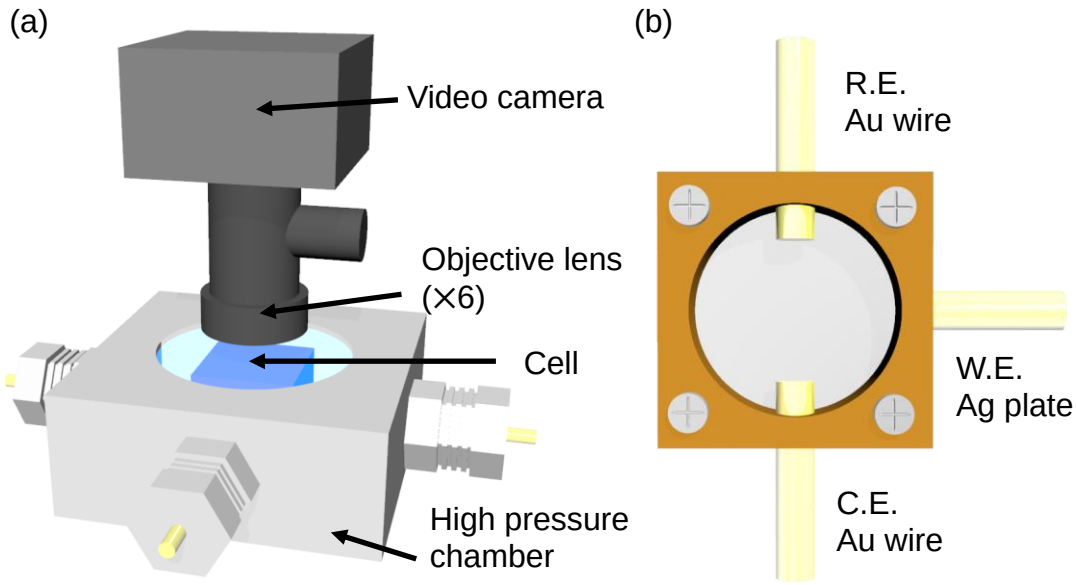

Figure 3.1. (a) Schematic structure of the video observation of H2 bubble observation system under electrochemical potential control. (b) Schematic structure of the cell vessel inside the high-pressure chamber.

3.3 Results and discussion

I evaluated the HER activity of the Ag electrodes from electrochemical measurements. Fig. 3.2 shows the linear sweep voltammograms of the Ag in 0.25 M Na_2SO_4 aqueous electrolytes under different hydrostatic pressure conditions. Slow scan rate, 5 mV s^{-1} was adopted for the evaluation of the steady state experiments[15,24] and to minimize the pH drift during the potentiostatic polarization.[25] The experiments were conducted by the setting the potential at 0 V versus RHE then cathodically sweeping of the potential to induce the HER. Video observation of the evolved H_2 bubbles were

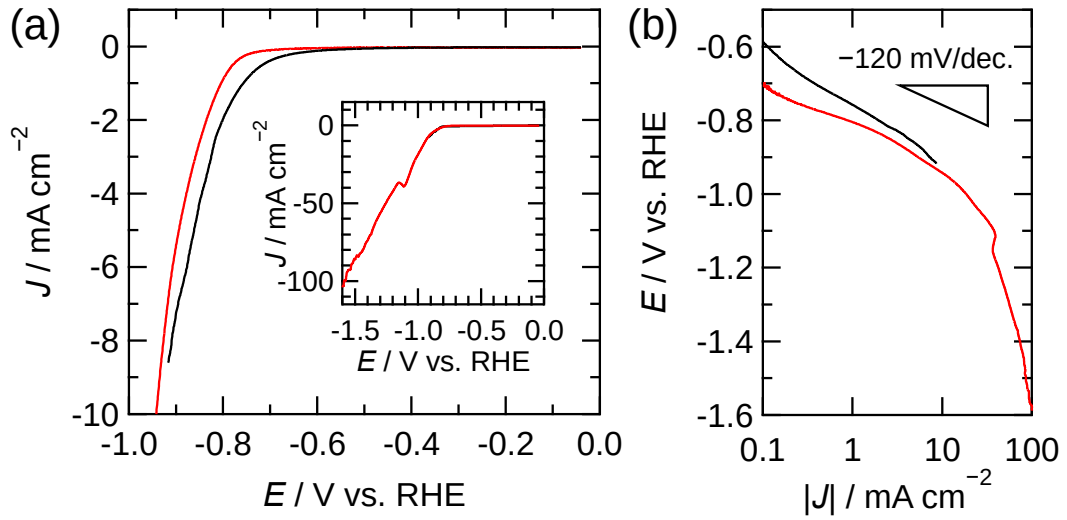

Figure 3.2. (a) Linear sweep voltammograms and (b) Tafel plots of Ag electrode in 0.25 M Na_2SO_4 aqueous solution electrolyte. Sweep rate was 5 mV s−1. Black trace represents 0.1 MPa as hydrostatic pressure. Red trace represents 75 MPa as hydrostatic pressure.

conducted during the electrochemical measurements as described afterwards. From the linear sweep voltammogram, the double-layer region was observed. Then cathodic currents were observed from around − 0.7 V versus RHE at 0.1 MPa. Similarly, in case with the 75 MPa, cathodic current was observed from − 0.8 V versus RHE as shown in Fig. 3.2a. For example, the overpotential of the − 5 mA cm^{-2} was − 0.86 V (0.1 MPa) versus RHE and − 0.91 V versus RHE (75 MPa), respectively. In both cases, the oscillation of the current behavior was observed in high overpotential region. In particular, the oscillation of the current density induced by bubble formations was observed from the − 0.9 V versus RHE at 0.1 MPa. Whereas the oscillation of the bubbles was observed from the − 1.3 V versus RHE at 75 MPa. These oscillations are due to the intensive H_2 bubble formation and detachments from the electrode. The Tafel slopes were analyzed by plotting the logarithm of current density and electrochemical potential of the working Ag electrodes (Fig. 3.2 b). The Tafel slope of HER from Ag in for 0.1 MPa was analyzed as the − 130 mV per decade. The Tafel slope of HER from Ag in for 75 MPa was analyzed as the − 110 mV per decade. The shown Tafel slopes of Ag are

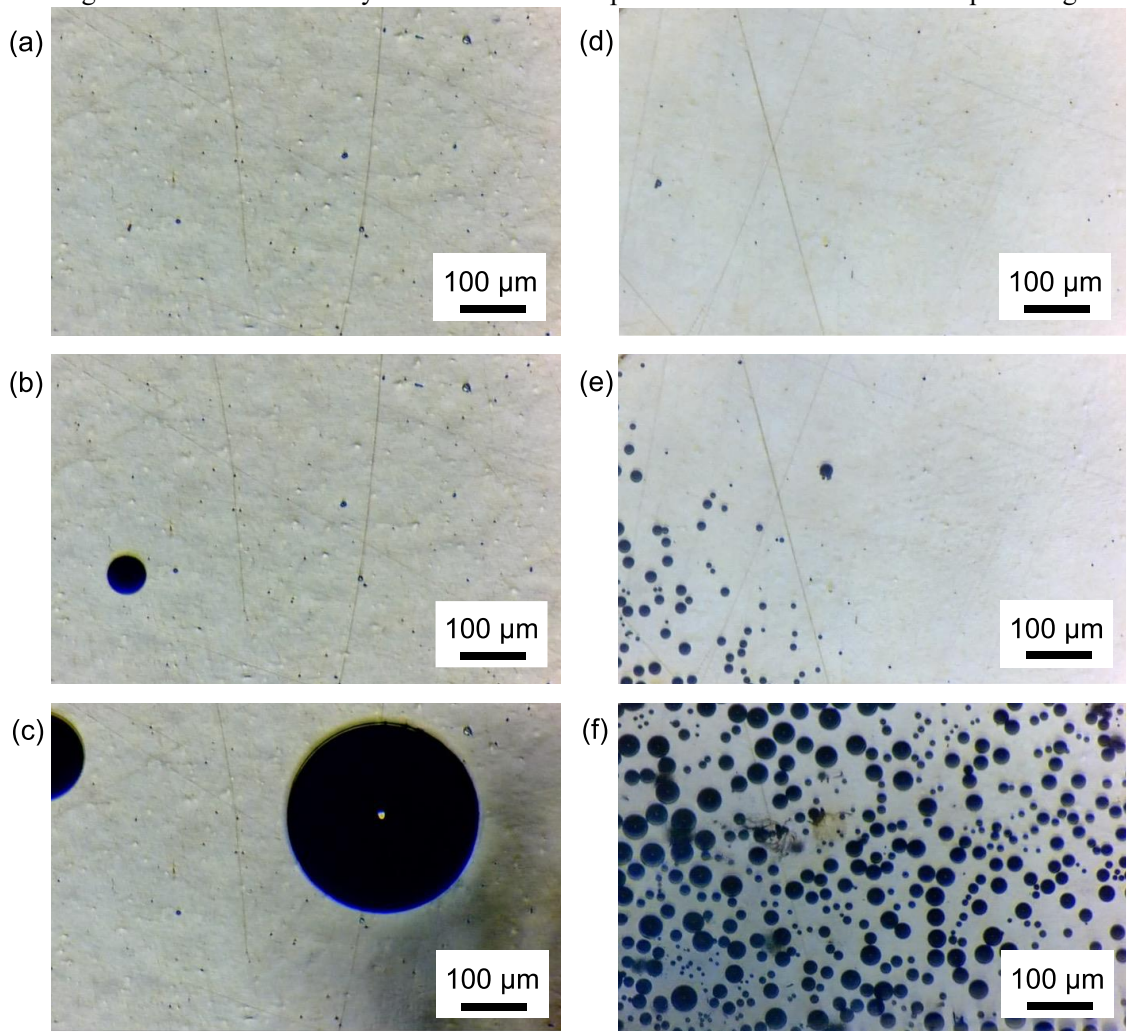

Figure 3.3. Representative snapshots of the bubble formation from Ag electrode in 0.25 M Na2SO4 aqueous solution with different pressure condition. (a) −0.05 V versus RHE, (b) −0.77 V versus RHE, and (c) −0.84 V versus RHE under 0.1 MPa. (d) −0.05 V versus RHE, (e) −1.25 V versus RHE, and (f) −1.55 V versus RHE under 75 MPa.

consistent with the Volmer step, where hydrogen atom transfer occurred from water molecules to bare Ag surface, as the rate-limiting step.[26]

The bubble formation was continuously tracked from the video observation in 0.1 MPa. The electrochemical potential was controlled during the video observation. Representative images of hydrogen bubble formation behavior were shown in Fig. 3.3a–c. The hydrogen bubbles start to grow around − 0.8 V. The size of the hydrogen bubbles range between 200 μm and 300 μm as the diameter. The detachments of the bubbles were also observed afterwards. Since the size of the bubbles was large, few bubbles were observed with the lower overpotential region. Many bubbles were observed in the high overpotential region. Continuously, large bubbles were formed. I also observed the bubble formation process in 75 MPa. Representative images of hydrogen bubble formation behavior in high pressure condition were shown in Fig. 3.3d–f. The hydrogen bubbles start to grow around − 1.25 V. The size of hydrogen bubbles grows up to 20 μm. The detachments of the bubbles were also observed afterwards. Since the size of the bubbles are small in high pressure conditions, many bubbles were observed even from the high-pressure condition. Apparently, the growth behavior of bubbles was dependent on the pressure conditions.

The bubble growth processes of H_2 were analyzed from the image analysis (Dipp-Macro II, DITECT). The time and size of the individual bubbles were tracked from the binarization of the image data of the video. The diameter of the bubble was analyzed from the area of the bubble as two-dimensional images. Then, the number of molecules by assuming the sphere on the bubbles. As discussed later, the exponential behavior of the number of H_2 molecules were also observed. Then, current density was calculated as differential of the number of H_2 molecules to time by assuming the two-electron Faradaic process.

Fig. 3.4 shows the HER bubble analyses with the different hydrostatic pressure conditions. The onset potentials of bubbles were dependent on the hydrostatic pressure conditions (Fig. 3.4a,d). In case with the 0.1 MPa, the onset potential for the bubble observation was around − 0.8 V versus RHE. On the other hand, in case with the 75 MPa, the onset potential for the bubble observation was around − 1.25 V. From the electrochemical measurements, the onset potential for the HER was comparable; − 0.86 V for 0.1 MPa and − 0.91 V for 75 MPa. The difference between electrochemical measurements and bubble observation is probably due to the high solubility of H2 in high pressure condition. Due to the Henry's law, the solubility of H_2 was increased from 0.5 mM (0.1 MPa) to 0.4 M (75 MPa) by increasing the hydrostatic pressure.[27-29] The higher solubility of the H_2 in aqueous electrolytes probably inhibits the nucleation of the bubbles by influence on the surface energy of the bubbles. The diameter of the bubbles were converted to the total amount of H_2 gas (Fig. 3.4b,e) by considering the density of the H_2 gas at given hydrostatic pressure condition[30]. The differential plot of the amount of H_2 gases can be converted to the current density from the bubble (J_{bubble}). The plot of logarithm of J_{bubble} and electrochemical potential gives the Tafel plots.

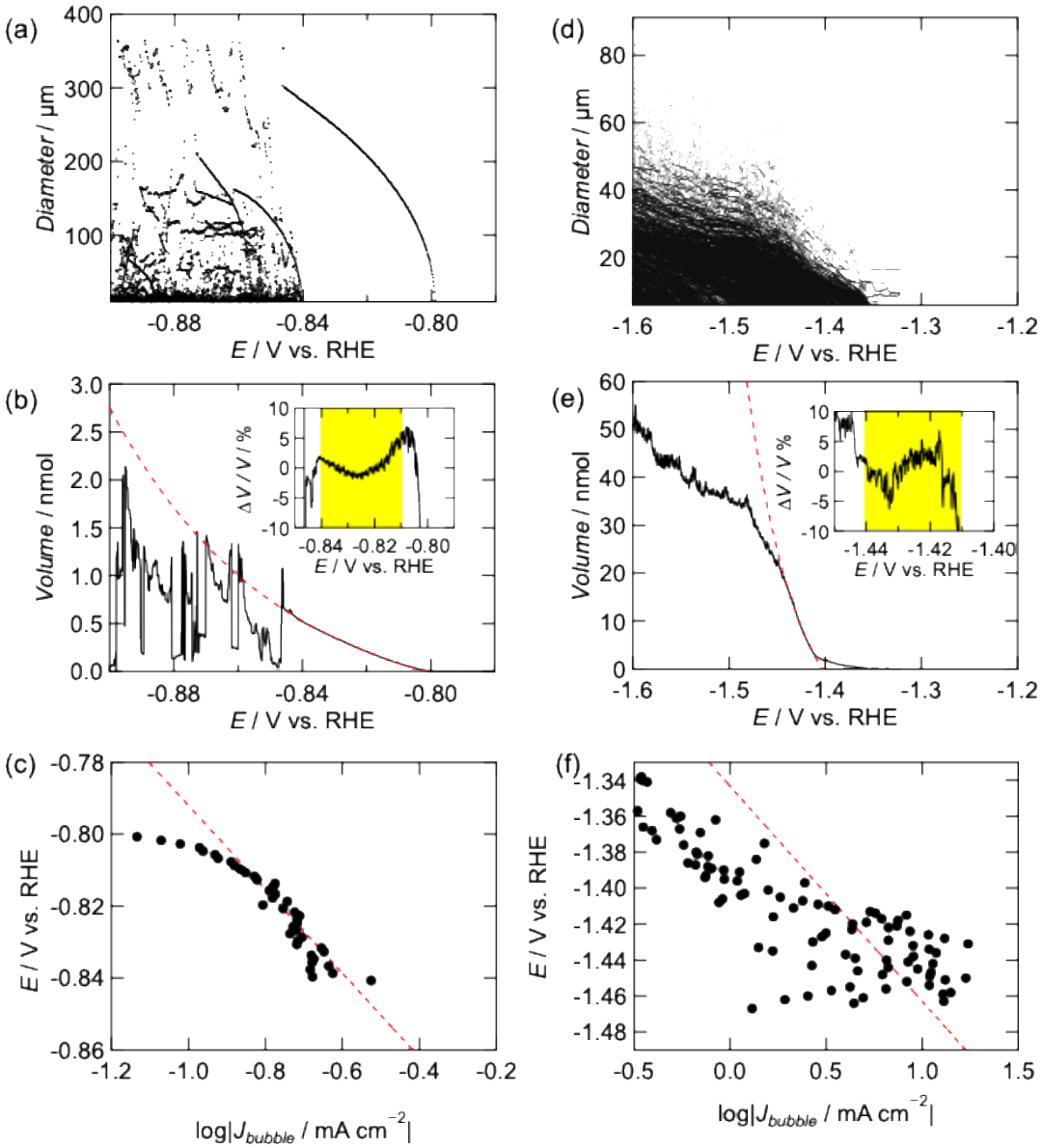

Figure 3.4. Quantitative analyses of HER behavior of Ag electrode in 0.25 M Na_2SO_4 aqueous solution with different pressure condition at (a, b, c) 0.1 MPa and (d, e, f) 75 MPa. (a, d) Growth of the diameter of the individual bubbles at given electrochemical potential. (b, e) Total volume of the bubbles at given electrochemical potential. Red dotted line represents the fitting to the experimental data. Inset shows the difference between the experiments and fitting. Yellow background region was used for the fitting. (c, f) Tafel plots from the current density calculated from the bubble. Red dotted lines represent the line adopted from Fig. 3.4b and e.

The Tafel analysis was conducted by following. By differentiating the volume per time gives the corresponding kinetics in the HER. However, due to the small difference in the size increments for the video observation, the noises in the J_{bubble} are relatively large for the linear fit. Therefore, I conducted the fitting to the dependence of the volume to the electrochemical potential, which corresponds to the Tafel fitting in the integrated form. The equation was shown in following.

$$n = n_0 + Aexp(-FE/\alpha RT) \qquad (23)$$

Where, n [mol] represents the amount of hydrogen, E is the electrochemical potential [V], F is the

Faradaic constant, and T is the absolute temperature. n_0, A and α are fitting parameter. α is related to the Tafel slopes: the observed Tafel slope is calculated as the $-60 \times \alpha$ mV per decade.

The Tafel fitting was conducted for both ambient pressure and high-pressure conditions. The fitting was conducted between − 0.81 V and − 0.84 V for the HER in 0.1 MPa as shown in Fig. 3.4b. Inset in Fig. 3.4b shows the difference in experimental and fitting volume divided by the experimental volume. The difference in the fitting is within 5 %. The corresponding Tafel line was shown in Fig. 3.4b and c. The corresponding Tafel slope was calculated to be − 116 mV per decade. Similarly, the fitting was conducted between − 1.41 V and − 1.44 V for the HER in 75 MPa as shown in Fig. 3.4 e and f Inset in Fig. 3.4e shows the difference in experimental and fitting volume divided by the experimental volume. The difference in the fitting is within 5 %. The corresponding Tafel line was shown in Fig. 3.4e and f. The corresponding Tafel slope was calculated to be − 120 mV per decade. In both cases, the fitting region is narrow in the range. In case with the lower overpotential region, the bubble nucleation process can influence on the analysis. In case with the higher overpotential in the range, the bubble detachments and intensive evolution can be problematic for the Tafel analysis. Interestingly even in the different pressure condition, the Tafel slope showed the − 120 mV per decade (Fig. 3.4c and f). This is typical value for the HER with the Volmer step as the rate-limiting step in the net reaction of HER. Importantly, these analyses can be both conducted around − 0.8 V and − 1.4 V versus RHE. Similar analyses were conducted for the flat Pt electrode The observed Tafel slopes were 34 mV per decade, which can be also typical behavior for the Tafel steps as a rate-limiting step.[26] These results showed that variation of pressure condition can modulate the bubble growth behavior leading to the good fit of the Tafel plots even from the video observation.

It has been reported that the bubble behavior is related to the bubble growth behavior is also related to the various processes.[31-34] Control over the bubble growth rate have been generally described in the form of following.

$$R = bt\beta R \qquad (24)$$

Where R is the bubble radius, t is the actual residence time of bubble. Here, b is the dimensional growth coefficient whereas β is the scaling exponent. The scaling exponent can be 1/2 or 1/3 depending on conditions. The condition fulfills the active electrode surface area, Ae, with the diameter of the bubbles at the detachment, Rd. (i) Surface-reaction-controlled growth for relatively small active electrode surfaces, $A\mathrm{e}/R\mathrm{d}^2 \ll 1$, where $R = bt^{1/3}$.[33,34] (ii) Diffusion-controlled growth for relatively large active electrode surface, $A\mathrm{e}/R\mathrm{d}^2 \gg 1$, where $R = bt^{1/2}$. [33,34] In my experiment, I utilized the flat electrode therefore $A\mathrm{e}/R\mathrm{d}^2 \gg 1$. In this case, diffusion-controlled growth behavior can be observed. Fig. 3.5 shows the comparison of the Tafel plot in the case with the simulation. I cannot observe the similarity from the bubble growth data.

The diameter of the bubbles can be described with the following equation in case with the diffusion-controlled reaction, $R = bt^{1/2}$. The volume of the gas can be calculated as following.

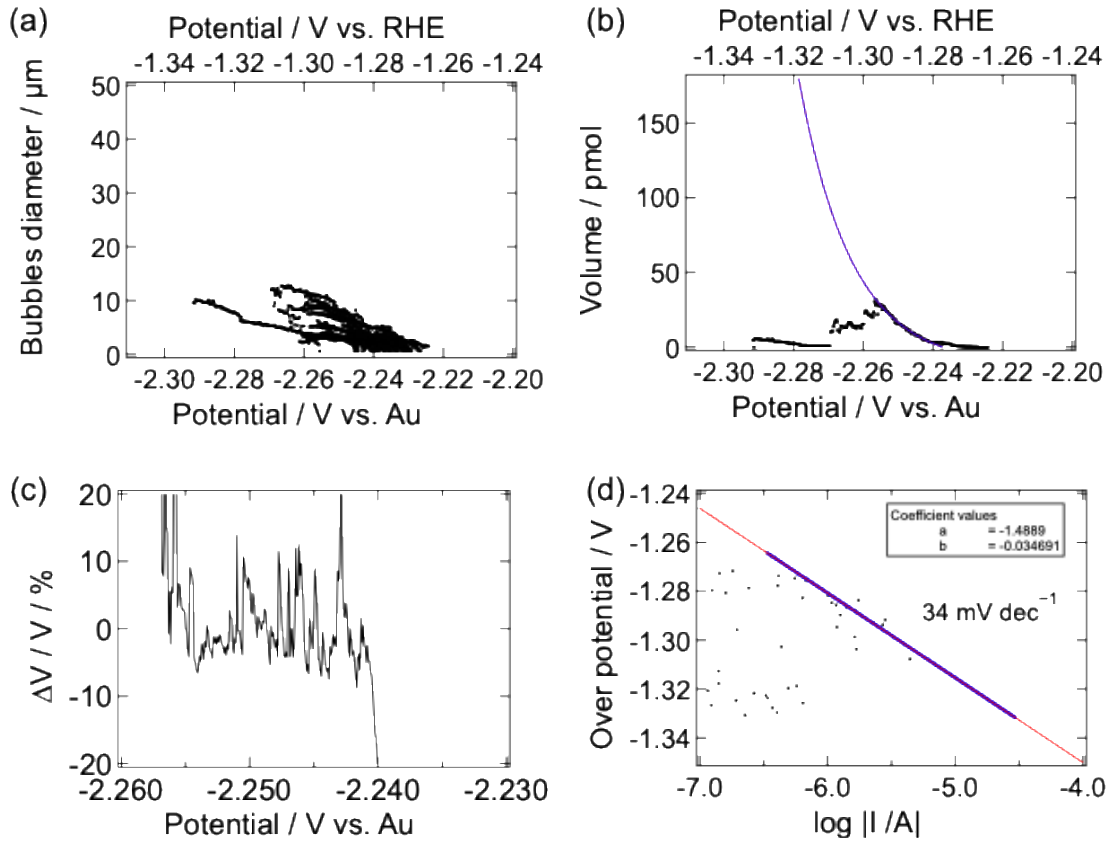

Figure 3.5. Quantitative analyses of HER behavior of Pt electrode in 0.25 M Na_2SO_4 at 75 MPa. (a) Growth of the diameter of the individual bubbles at given electrochemical potential. (b) Amount of the total bubbles at given electrochemical potential. (c) Linear sweep voltammogram from the bubbles. (d) Tafel plots from the current density calculated from the bubble. Red line represents the fitting to the experimental data.

$$V = \frac{\pi}{6}R^3 = \frac{\pi b^3}{6}t^{3/2} \qquad (25)$$

In case with the linear sweep voltammogram, the potential can be proportional to the time. The current density can be proportional to the volume of gases. Therefore, current density can be described as following. Therefore, the current density for the diffusion-limited region shows dependence on the time.

$$J \propto \frac{dV}{dt} = \frac{\pi b^3}{4}t^{1/2} \qquad (26)$$

In case with the derivation with the Tafel plot, the equation can be described as following.

$$\log|J| = constant + \frac{1}{2}\log(t) = constant + \frac{1}{2}\log|E| \qquad (27)$$

The plotted data were compared with the experimentally obtained data as shown in Fig. 3.6.

The formation of bubbles can be thought as the sequential process. First, there are no hydrogen molecules around the Ag electrode–electrolyte interface. Due to the cathodic HER, the hydrogen molecules were produced around the electrode–electrolyte interface. Since the solubility of the hydrogen molecules is limited to the 0.5 mM in electrolyte solution at 0.1 MPa at room

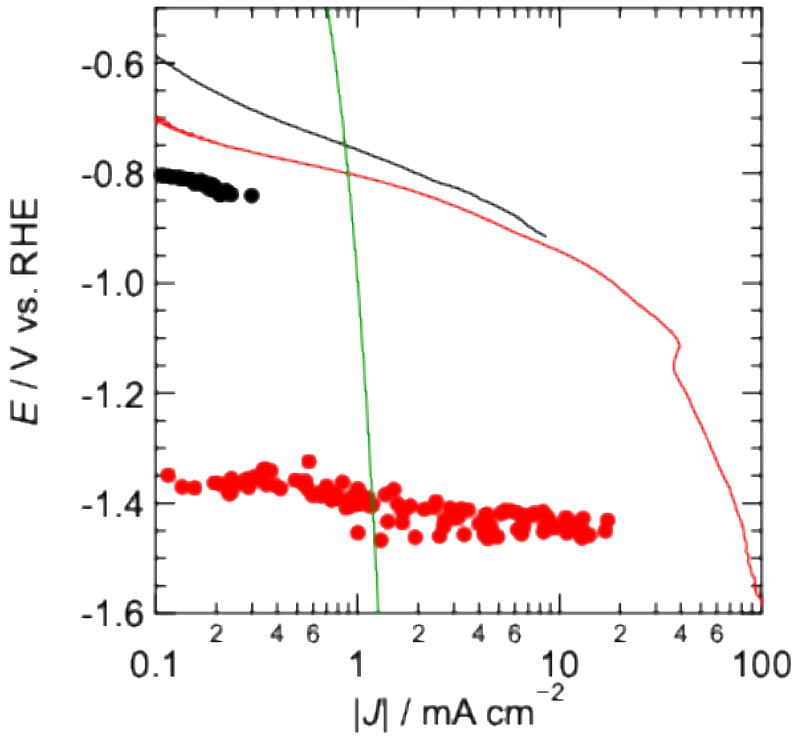

Figure 3.6. Tafel plots of Ag electrode in 0.25 M Na_2SO_4 electrolyte from linear sweep voltammogram (solid lines). Tafel plots from the current density calculated from the bubble (filled circles). Black trace represents 0.1 MPa as hydrostatic pressure. Red trace represents 75 MPa as hydrostatic pressure. Sweep rate was 5 mV s^{-1}. Green line represents the diffusion-controlled growth process.

temperature[27,35,36], the solubility limits induce the faster nucleation of the hydrogen bubbles. On the other hand, higher solubility of the hydrogen molecules at 75 MPa, the slower nucleation leads to the multiple bubble nucleation process leading to the narrower size distribution of the bubbles. The bubble was attached to the electrode and local hydrogen was transferred from the liquid phase to gas phase to grow the size of the bubbles. The hydrogen bubbles were grown upon the increase of the rate of the electrode reaction, which can be analyzed with the Tafel analysis as shown in Fig. 3.4c and f. The hydrogen bubbles can be detached due to the unbalancing the buoyancy and aerophobic force at the electrodes.

The bubble behavior is still discussed based on the gradients around the bubbles.[19] Koper et al. explained about the solute-dominant regime or thermal dominant regime for the bubble formation. Usually, high current density region is dominated by the thermal dominant region for the bubble formation. The thermal dominant region can be difficult to analyze the bubble behavior due to the difference in the surface tension at the local bubbles. However, by applying the high pressure, the bubble behavior can be attenuated. I assume that bubble behavior can be solute-dominant regime. This can be the reason why I can analyze the Tafel plots even in the range of high overpotential.

Finally, I would like to discuss about the use of the methodology for the evaluation of the electrochemical behavior at high overpotential region. Fig. 3.7 shows the correlation of the current density from the electrochemical measurements and bubble observation. Faradaic efficiency of the

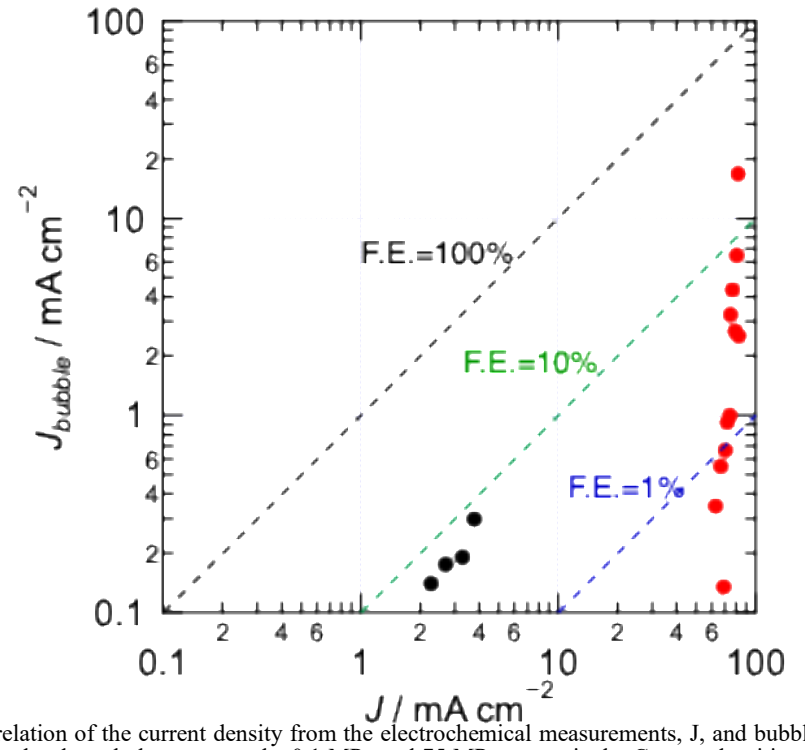

Figure 3.7. Correlation of the current density from the electrochemical measurements, J, and bubble analysis, J_{bubble}. Black symbols and red symbols represent the 0.1 MPa and 75 MPa respectively. Current densities were plotted from −0.81 V to −0.84 V for 0.1 MPa. Current densities were plotted from −1.36 V to −1.46 V for 75 MPa. Faradaic efficiency (F.E.) for the bubble production was plotted for the eye-guide.

bubble formation is below 100 % in general. This is probably due to the diffusion of the H_2 from the electrode surface without the bubble formation. For example, under the hydrostatic pressure of 0.1 MPa, the Faradaic efficiency of was between the range of 5 % and 8 %. On the other hand, under the hydrostatic pressure of 75 MPa, the Faradaic efficiency of was between the range of 0.5 % and 17 %. The increase of Faradaic efficiency can be probably due to the intensive HER behavior for higher overpotential range. At ambient pressure condition, it can be useful to track HER behavior with similar Faradaic efficiency. On the other hand, high pressure condition can be useful for the evaluation of the electrocatalytic behavior in high overpotential conditions. These unique characteristics can be useful for the evaluation of the electrocatalytic behavior in different overpotential range.

3.4 Conclusions

In this study, I developed the methodology for the evaluation of the HER activity from the bubble observation under electrochemical potential control. I used Ag electrode with different pressure conditions. I successfully observed the bubble growth of the H_2 bubbles under electrochemical potential control. The image analyses were utilized for the evaluation of the HER behavior even for the Tafel plots. The data analyzed showed 120 mV per decade as a Tafel slope, which was typical value for the Volmer mechanism as the rate-limiting step. This study opens the opportunity for the utilization of bubble observation as the descriptor for the evaluation of electrocatalytic activity as

the rapid analytical methods for new material discovery.

3.5 References

1. Kita, H. Periodic Variation of Exchange Current Density of Hydrogen Electrode Reaction with Atomic Number and Reaction Mechanism. *J. Electrochem. Soc.* **113**, 1095 (1966).
2. Trasatti, S. Work function, electronegativity, and electrochemical behaviour of metals. *J. Electroanal. Chem. Interfacial Electrochem.* **39**, 163–184 (1972).
3. McCrory, C. C. L., Jung, S., Peters, J. C. & Jaramillo, T. F. Benchmarking heterogeneous electrocatalysts for the oxygen evolution reaction. *J. Am. Chem. Soc.* **135**, 16977–16987 (2013).
4. McCrory, C. C. L. *et al.* Benchmarking Hydrogen Evolving Reaction and Oxygen Evolving Reaction Electrocatalysts for Solar Water Splitting Devices. *J. Am. Chem. Soc.* **137**, 4347–4357 (2015).
5. Bockris, J. O. & Potter, E. C. The mechanism of the cathodic hydrogen evolution reaction. *J. Electrochem. Soc.* **99**, 169 (1952).
6. Jackson, M. N. & Surendranath, Y. Donor-Dependent Kinetics of Interfacial Proton-Coupled Electron Transfer. *J. Am. Chem. Soc.* **138**, 3228–3234 (2016).
7. Jackson, M. N., Jung, O., Lamotte, H. C. & Surendranath, Y. Donor-Dependent Promotion of Interfacial Proton-Coupled Electron Transfer in Aqueous Electrocatalysis. *ACS Catal.* **9**, 3737–3743 (2019).
8. Dubouis, N. & Grimaud, A. The hydrogen evolution reaction: From material to interfacial descriptors. *Chem. Sci.* **10**, 9165–9181 (2019).
9. Minamimoto, H., Osaka, R. & Murakoshi, K. In-situ observation of isotopic hydrogen evolution reactions using electrochemical mass spectroscopy to evaluate surface morphological effect. *Electrochim. Acta* **304**, 87–93 (2019).
10. Fukushima, T., Ashizawa, D. & Murakoshi, K. Rapid detection of donor-dependent photocatalytic hydrogen evolution by NMR spectroscopy. *RSC Adv.* **12**, 12967–12970 (2022).
11. Sato, D., Minamimoto, H. & Murakoshi, K. Plasmon-induced Hydrogen Evolution Reaction on p-Type Semiconductor Electrode with Ag Nanodimer Structures. *Chem. Lett.* **49**, 806–808 (2020).
12. van der Heijden, O., Park, S., Eggebeen, J. J. J. & Koper, M. T. M. Non-Kinetic Effects Convolute Activity and Tafel Analysis for the Alkaline Oxygen Evolution Reaction on NiFeOOH Electrocatalysts. *Angew. Chemie - Int. Ed.* **62**, 1–9 (2023).
13. Fujimura, T., Hikima, W., Fukunaka, Y. & Homma, T. Analysis of the effect of surface wettability on hydrogen evolution reaction in water electrolysis using micro-patterned electrodes. *Electrochem. commun.* **101**, 43–46 (2019).
14. Zheng, W. iR Compensation for Electrocatalysis Studies: Considerations and Recommendations. *ACS Energy Lett.* **8**, 1952–1958 (2023).

15. van der Heijden, O., Park, S., Vos, R. E., Eggebeen, J. J. J. & Koper, M. T. M. Tafel Slope Plot as a Tool to Analyze Electrocatalytic Reactions. *ACS Energy Lett.* **9**, 1871–1879 (2024).
16. Yuan, S. *et al.* Bubble evolution and transport in PEM water electrolysis: Mechanism, impact, and management. *Prog. Energy Combust. Sci.* **96**, 101075 (2023).
17. de Jonge, R. M., Barendrecht, E., Janssen, L. J. J. & van Stralen, S. J. D. Gas bubble behaviour and electrolyte resistance during water electrolysis. *Int. J. Hydrogen Energy* **7**, 883–894 (1982).
18. Qiu, H. *et al.* Quantitative Description of Bubble Formation in Response to Electrolyte Engineering. *Langmuir* **39**, 4993–5001 (2023).
19. Park, S. *et al.* Solutal Marangoni effect determines bubble dynamics during electrocatalytic hydrogen evolution. *Nat. Chem.* **15**, 1532–1540 (2023).
20. ANKETELL, J. & LEARNER, R. C. M. Kinetics of Electrolytic Hydrogen and Deuterium Evolution. *Proc. Roy. Soc. London. Ser. A. Math. Phys. Sci.* **256**, 128–144 (1960).
21. Ammar, I. A. & Awad, S. A. Hydrogen overpotential on silver in sodium hydroxide solutions. *J. Phys. Chem.* **60**, 1290–1293 (1956).
22. M.A.V. Devanathan, J.O'M. Bockris, W. M. The degree of coverage of silver cathodes with adsorbed atomic hydrogen during hydrogen evolution in alkaline solutions. *J. Electroanal. Chem.* **1**, 143–160 (1959).
23. Antoniou, A. A. & Wetmore, F. E. W. Cathodic Polarization of Silver in Sulphuric Acid. *Can. J. Chem.* **37**, 222–227 (1959).
24. Anantharaj, S., Noda, S., Driess, M. & Menezes, P. W. The Pitfalls of Using Potentiodynamic Polarization Curves for Tafel Analysis in Electrocatalytic Water Splitting. *ACS Energy Lett.* **6**, 1607–1611 (2021).
25. Auinger, M. *et al.* Near-surface ion distribution and buffer effects during electrochemical reactions. *Phys. Chem. Chem. Phys.* **13**, 16384–16394 (2011).
26. Shinagawa, T., Garcia-Esparza, A. T. & Takanabe, K. Insight on Tafel slopes from a microkinetic analysis of aqueous electrocatalysis for energy conversion. *Sci. Rep.* **5**, 13801 (2015).
27. C.L. Young. *SOLUBILITY DATASERIES, Hydrogen and deuterium*. vols 5, 6 (IUPAC Solubility Data Series, Pergamon Press, 1981).
28. Wiebe, R., Gaddy, V. L. & Heins, C. Solubility of Hydrogen in Water at 250c from 25 to 1000 Atmospheres. *Ind. Eng. Chem.* **24**, 823–825 (1932).
29. Wiebe, R. & Gaddy, V. L. The Solubility of Hydrogen in Water at 0, 50, 75 and 100° from 25 to 1000 Atmospheres. *J. Am. Chem. Soc.* **56**, 76–79 (1934).
30. Elberry, A. M., Thakur, J., Santasalo-Aarnio, A. & Larmi, M. Large-scale compressed hydrogen storage as part of renewable electricity storage systems. *Int. J. Hydrogen Energy* **46**, 15671–15690 (2021).
31. Van Der Linde, P. *et al.* Electrolysis-Driven and Pressure-Controlled Diffusive Growth of

Successive Bubbles on Microstructured Surfaces. *Langmuir* **33**, 12873–12886 (2017).

32. Iwata, R. *et al.* Bubble growth and departure modes on wettable/non-wettable porous foams in alkaline water splitting. *Joule* **5**, 887–900 (2021).
33. Verhaart, H. F. A., de Jonge, R. M. & van Stralen, S. J. D. Growth rate of a gas bubble during electrolysis in supersaturated liquid. *Int. J. Heat Mass Transf.* **23**, 293–299 (1980).
34. Wang, Y., Hu, X., Cao, Z. & Guo, L. Investigations on bubble growth mechanism during photoelectrochemical and electrochemical conversions. *Colloids Surfaces A Physicochem. Eng. Asp.* **505**, 86–92 (2016).
35. Ruetschi, P. & Amlie, R. F. Solubility of hydrogen in potassium hydroxide and sulfuric acid. Salting-out and hydration. *J. Phys. Chem.* **70**, 718–723 (1966).
36. Timofejew, W. Über die Absorption von Wasserstoff und Sauerstoff in Wasser und Alkohol. *Zeitschrift für Phys. Chemie* **6U**, 141–152 (1890).

4 Polaritonic Modification of Hydrogen Evolution Reaction under Dark

4.1 Introduction

Physicochemical properties of molecules can be modulated through the polariton formation under strong electromagnetic field. Recent advances in polaritonic chemistry have been demonstrated with the modification of chemical landscape.[1] Recently, theoretical prediction on the electron transfer reaction under strong electromagnetic confinements.[2,3] In case with the electrode surface, it is expected that the vacuum field can be quantized upon the structuring of electrode in nanoscale, which is known as plasmonic excitation under light illumination condition.[4,5] There are several reports on the enhancement of electron transfer reaction at nanostructured electrode system.[6,7] However, due to the lack of the systematic demonstration, it is still hard to quantify the effect of nanostructure on the electrocatalytic behavior. Here, I studied systematic study of the effect of Ag nanostructure on the electrocatalytic activity on hydrogen evolution reaction. The Ag nanostructures were prepared by electron beam lithography. The electrocatalytic HER behavior was investigated from the bubble analysis from the imaging of evolved hydrogen from the nanostructured electrodes. I investigated that the overpotential of the HER can be enhanced over 0.4 V. In addition, from the detailed analysis on the Tafel slope of the bubble behavior the Tafel slope was decreased to the even 30 mV per decade, which cannot be explained by the classical mechanism of HER. Upon the consideration of microkinetic model under strong electromagnetic field condition, the behavior can be explained in the context of the modification of the reaction pathway. In addition, the isotopic experiment revealed that the tunneling effect can be even enhanced associated with the quality factor of the resonance in nanostructured electrode.

4.2 Experiments

Fabrication on substrates

A glassy carbon electrode (GC) was immersed in aqua regia with a volume ratio of 3:1 hydrochloric acid and nitric acid for 1 hour for cleaning, then rinsed three times with ultrapure water and boiled three times. It was then polished with diamond slurry (diameter = 1 μm) for 5 minutes. The electrode was further cleaned in ethanol under ultrasonic treatment for 10 minutes to remove the residual diamond slurry. The electrode was polished again with diamond slurry (diameter = 0.25 μm)) for 5 minutes. The electrode was further cleaned in ethanol under ultrasonic treatment for 10 minutes to remove the residual diamond slurry. The electrodes were stored in fresh ethanol. The GC was placed on a hot plate kept at 130 °C, and the ethanol was completely removed. A resist solution of ZEP520A and ZEP-A mixed at a ratio of 2:1 was applied by spin coating at 300 rpm for 3 seconds and 4000 rpm for 60 seconds. Nanopatterns were then drawn using electron beam lithography (ELS-F130, ELIONIX). The substrate was then immersed in ZED-N50 for 60 seconds, and then swung in ZMD-B at a speed of one round trip per second over a space of about 3 cm for 10 seconds. The rinse

solution was then immediately removed with N_2 gas. Ag was deposited on the developed substrate at a deposition rate of 0.1 nm s^{-1} using an electron beam evaporator. The resist was removed by immersing the substrate in N,N-dimethylacetamide solution. If the resist could not be sufficiently removed, ultrasonic cleaning was performed in the solution at a reduced output.

Electrochemical measurement

A three-electrode inner cell was constructed using the substrate (Fig. 4.1d) prepared above as the working electrode, an Au wire as the counter electrode, and an Au wire as the quasi-reference electrode. 0.25 M Na_2SO_4aq. was used as the electrolyte solution. This inner cell was placed in a high-pressure chamber, and the pressure in the system was set to 75 MPa by injecting silicone oil using a hydraulic valve. At this time, the pressure in the high-pressure chamber was transmitted to the inside of the inner cell through a silicone tube at the top of the inner cell. A camera for video recording was placed on top of the high-pressure electrochemical cell constructed in this way. The electrochemical conditions were Linear Sweep Voltammetry (LSV) with a sweep rate of −5 mV s^{-1}, and the occurrence and growth of bubbles on the surface linked to the electrochemical information was observed with the camera at the same time as the electrochemical measurement (Fig. 4.1a,b). Isotopic mixture aqueous solutions were used as the solvent this time. The D_2O concentration were 0%, 10%, 90%, and 100% by weight.

Ag (diameter = 7.0 mm) was immersed in perchloric acid for 30 minutes, rinsed three times with ultrapure water, boiled three times, and polished in the same way as for GC. It was then washed

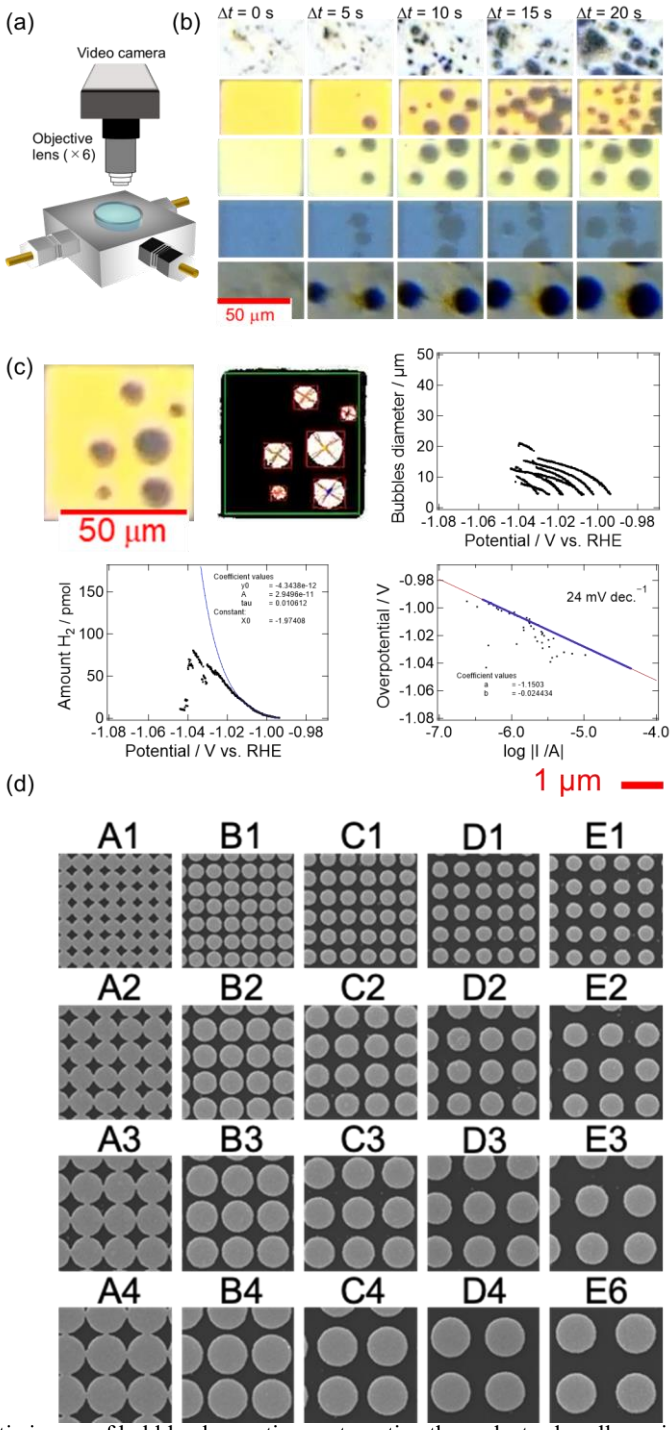

Figure 4.1. (a) Schematic image of bubble observation system, tine three electrode cell was in high pressure chamber, (b) Image of bubbles formation and growth on Pt plate, nano-structured Ag and Ag plate. From upper Pt plate, high, middle, low nano-Ag, Ag plate in 0.25 M Na_2SO_4aq. Content of D_2O was 0%. (c) Flows of bubble analysis, bubble image and binarization between bubble and background, bubble diameter, amount of H_2 gas and Tafel plot under LSV measurement using bubble analysis (d) SEM images of nano structures on GC electrode, gray was Ag and black was GC.

again with perchloric acid to obtain a mirror-like Ag plate. An inner cell was constructed using this Ag plate as the working electrode and Au as the counter electrode and pseudo-reference electrode. Linear sweep voltammogram (LSV) and video of bubble generation under high pressure were

obtained. A Pt (ϕ = 7.0 mm) plate was also immersed in a 1:1 volumetric mixture of sulfuric acid and nitric acid for 30 minutes. It was rinsed three times with pure water, boiled three times, polished in the same way, and washed again with the mixed acid. The same experiment as for the Ag plate was conducted using this substrate as the working electrode. In addition, as a method of potential correction for the pseudo reference electrode, a similar LSV measurement was performed with an Ag wire as the working electrode, and an LSV measurement was performed using a similar electrolyte solution by constructing a three-electrode electrochemical cell at normal pressure with an Ag wire as the working electrode, a Pt black wire as the counter electrode, and a handmade Ag/AgCl sat. KCl as the reference electrode. The potential of the pseudo reference electrode was determined by comparing the fall potential of the HER from the two experimental results.

The C2 structure (ϕ = 600 nm, a = 750 nm) was fabricated by EBL over an area of 1 mm × 1 mm. A three-electrode cell was constructed with this substrate as the working electrode, Pt black as the counter electrode, and Ag/AgCl as the reference electrode. 0.25 M Na_2SO_4 aqueous solution was used as the electrolyte solution. The isotope mixing ratio was 0%. LSV was performed with the sweep rate of −5 mV s^{-1}. For comparison, a GC substrate with Ag evaporated over the entire surface, an Ag plate, was used. In addition, a rotating disk electrode was used for the LSV measurement to remove evolved bubbles (1200 rpm).

Analysis of bubble videos

Bubble generation and growth are not caused by electron transfer alone, but are governed by various factors such as bubble nucleation from surface saturation, changes in interfacial energy depending on bubble size, and diffusion of hydrogen molecules generated near the electrode due to time changes.[8] In this experiment, in order to confirm that bubble growth is caused by electron transfer reaction, image analysis was performed on the bubble growth video. Fig. 4.1c (see Appendix) shows, from the left, a snapshot of the video, a binarized version of the snapshot, the bubble size obtained from the binarized data, the number of moles in the bubble calculated from the bubble size (the total value if there are multiple bubbles), and the current value was calculated by differentiating this approximation curve with respect to time. This allowed us to obtain a Tafel plot that shows the relationship between the logarithm of the current and the potential. The slope of the Tafel plot is important as an index of electrochemical activity and as an index of the reaction mechanism, so I also calculated it. The electron transfer reaction at the electrode can be described by considering the potential dependence of the rate constant, and the current value increases with exp against the overpotential. In this result, if the change in the number of moles on the nanostructure surface depends on electron transfer, the amount of change is considered to be exp with respect to the potential. In fact, the plot of the number of moles in the center of Fig. 4.1c can be divided into three regions. (i) The initial region where bubble nucleation does not cause bubble growth and remains

flat. Here, the surface energy and (ii) the middle region where the number of moles change to exp according to the theory of bubble nucleation. (iii) The late region where physical phenomena other than electron transfer reactions occur, such as bubble association, diffusion of hydrogen molecules, interfacial energy due to large bubble size, solution removal due to increased bubble size, and convection. In this case, it follows exp in the middle region. In this case, since it follows exp in the middle region, an approximation curve was drawn in this region (about 20-40 mV) using the following formula.

$$n\,[\mathrm{mol}] = n_0 + A\exp\left(-\frac{E - E_0}{t}\right) \tag{28}$$

4.3 Results and discussion

The image analysis results of Fig. 4.1c were performed for each metal nanostructure, and the results are summarized as current-potential curves in Fig. 4.2. Each number indicates the D_2O ratio. In addition, letters such as A1 in the graph indicate each metal nanostructure (structures where no bubbles were generated during video recording or where image analysis was impossible have been

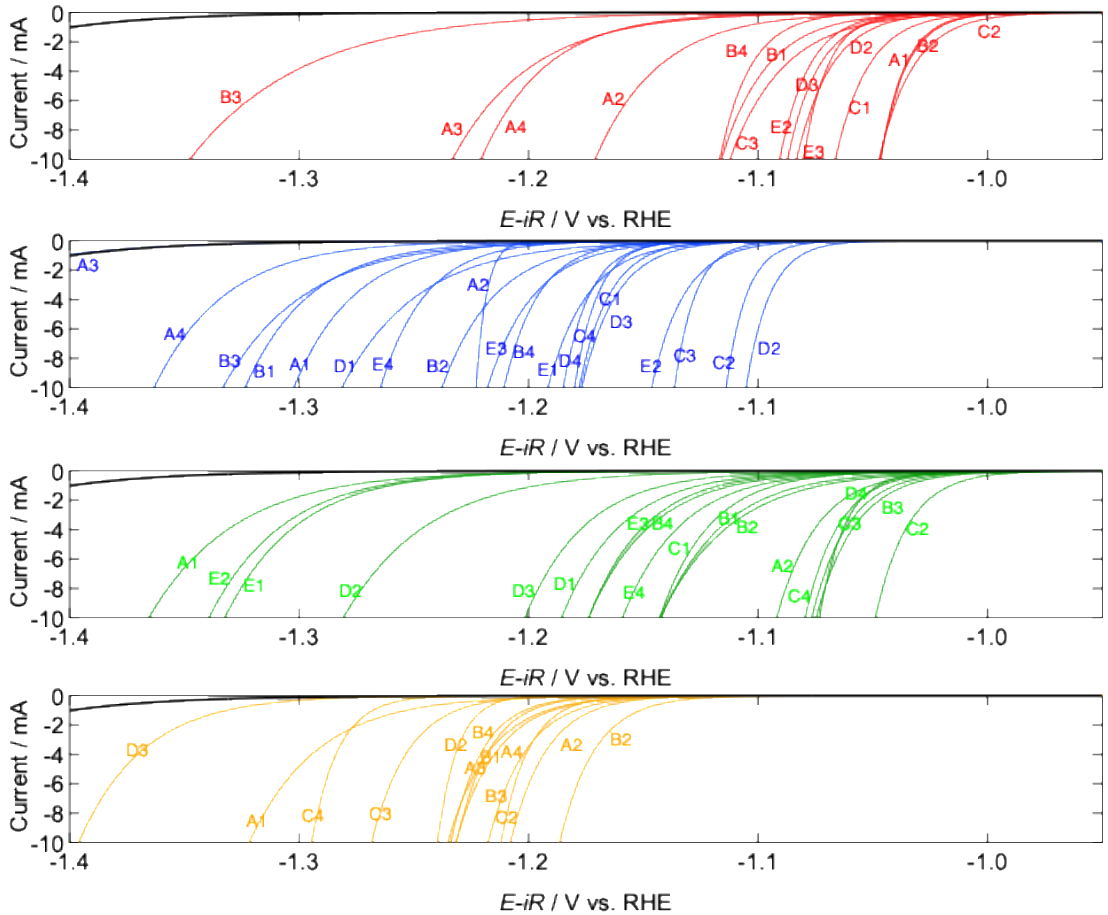

Figure 4.2 I-V curves by bubble analysis, the numbers on top left indicate content of D_2O and alphanumeric characters indicate identification number of nanostructures. The left and right black curve of graphs indicate result of Ag plate and Pt plate bubbles in 0% D_2O solution, respectively.

excluded). Furthermore, the left and right black lines in all graphs are the results for Ag plate and Pt plate with 0% isotope mixing ratio, respectively. It has long been known that H_2O and D_2O show different reactivity in electrochemical HER on a flat electrode.[9] However, this is simply because the overpotential is larger because additional energy is required for the reaction of D_2O compared to the reaction of H_2O.[10] In other words, the current-potential curve simply shifts in the potential direction. When HER occurs with an isotope mixed solution on a normal electrode, the activity decreases in the order of 0% > 10% > 90% > 100%. First, the I-V curves vary depending on the metal nanostructure, and it is clear that there is a difference in activity depending on the metal nanostructure. It is also clear that the activity is greater in all metal nanostructures compared to the Ag Plate. This is true not only for the 0% result, but also for 100%. It can be said that the modulation of activity due to the metal nanostructure is greater than the modulation of activity due to the isotope. For example, in terms of energy, the energy change due to the strong binding state with the metal nanostructure is greater than the energy difference of the zero-point energy of the isotope. Compared to a normal electrode, the electrode using this metal nanostructure shows a different order of activity for each metal nanostructure under each isotope mixing condition. For example, the five most active structures are C2>B2>A1>C1>D2 at 0%, D2>C2>C3>E2>D3 at 10%, C2>B3>C3>D4>C4 at 90%, and B2>A2>C2>B3>A4 at 100%. The reason for this change in order is thought to be that the molecules, intermediates, or transition states that resonate with the metal nanostructure are different. At present, it is unclear which state is resonating, but we can make some assumptions about this, as I will explain next.

Microkinetic modeling under strong cavity coupling

Microkinetic modeling is useful for understanding multiple proton-coupled electron transfer reactions.[11] We used it to study the impact of strong coupling on the hydrogen evolution reaction.

Case 1 : hydrogen evolution reaction without strong coupling

The half reactions for hydrogen evolution from metal M under basic or neutral conditions are

$$M + H_2O + e^- \rightarrow M\text{–}H + OH^- \quad (29)$$

$$M\text{–}H + H_2O + e^- \rightarrow M + H_2 + OH^- \quad (30)$$

$$M\text{–}H \rightarrow M + 0.5\ H_2 \quad (31)$$

The metal surface can react with water molecules to produce surface-adsorbed hydrogen, M–H (Volmer step; Eq. 29). Surface-adsorbed hydrogen can react with water molecules to produce H_2 (Heyrovsky step; Eq. 30) or recombine to produce H_2 (Tafel step; Eq. 31). In general, the kinetic constants for the forward (k_f) and backward (k_b) processes of the adsorption reaction can be written

$$k_f = k^0 \exp\left[-\frac{\alpha F(E-E_0)}{RT}\right] \quad (32)$$

$$k_b = k^0 \exp\left[\frac{(1-\alpha)F(E-E_0)}{RT}\right], \quad (33)$$

where the abbreviations are defined as follows: k^0, kinetic constant for exchange reaction; α, symmetry factor; E, electrochemical potential; E_0, equilibrium potential; R, ideal gas constant. The forward and backward reactions of reversible single electron transfer are described by the Butler–Volmer equation

$$j = j_0 \left\{ \exp\left[\frac{-\alpha n F(E-E_0)}{RT}\right] - \exp\left[\frac{(1-\alpha)F(E-E_0)}{RT}\right] \right\}, \quad (34)$$

where j is the current density, j_0 is the exchange current density, and n is the number of electrons involved in the electrode reaction. When the surface adsorption reaction is at equilibrium, the surface coverage, θ, of hydrogen is given by

$$\theta = \frac{KC_{\mathrm{H2O}}\exp\left[-\frac{F(E-E_0)}{RT}\right]}{1+KC_{\mathrm{H2O}}\exp\left[-\frac{F(E-E_0)}{RT}\right]} \quad , \quad (35)$$

where C_{H2O} is the concentration of water and K is the equilibrium constant.

The reaction kinetics of the Volmer, Heyrovsky, and Tafel steps can be calculated using microkinetic modeling. Since the Volmer and Heyrovsky steps are electrochemical reactions, the corresponding kinetic constants should be dependent on the electrochemical potential (Eqs. 32 and 33). Being a chemical reaction, the kinetic constant of the Tafel step does not on the electrochemical potential, but the surface coverage does. The reaction kinetics for the Volmer (r_{V}), Heyrovsky (r_{H}), and Tafel (r_{T}) steps are given by

$$r_{\mathrm{V}} = k_{\mathrm{V}} C_{\mathrm{H2O}}(1-\theta) = \frac{k_{\mathrm{V}}^0 C_{\mathrm{H2O}}\exp\left[-\frac{\alpha F(E-E_0)}{RT}\right]}{1+KC_{\mathrm{H2O}}\exp\left[-\frac{F(E-E_0)}{RT}\right]} \quad (36)$$

$$r_{\mathrm{H}} = k_{\mathrm{H}} C_{\mathrm{H2O}}\theta = \frac{k_{\mathrm{H}}^0 K C_{\mathrm{H2O}}^2\exp\left[-\frac{(1+\alpha)F(E-E_0)}{RT}\right]}{1+KC_{\mathrm{H2O}}\exp\left[-\frac{F(E-E_0)}{RT}\right]} \quad (37)$$

$$r_{\mathrm{T}} = k_{\mathrm{T}}\theta^2 = k_{\mathrm{T}}\left\{\frac{KC_{\mathrm{H2O}}\exp\left[-\frac{F(E-E_0)}{RT}\right]}{1+KC_{\mathrm{H2O}}\exp\left[-\frac{F(E-E_0)}{RT}\right]}\right\}^2, \quad (38)$$

where k_{V}, k_{H}, and k_{T} are the reaction kinetic constants for the Volmer, Heyrovsky, and Tafel steps, respectively, and k_{V}^0, and k_{H}^0, and k_{T}^0 are the corresponding exchange reaction kinetic constants. Under the strong coupling conditions, the rate of the kinetic rate can be expressed as following.

$$k_{\mathrm{sc}} = \frac{2\pi}{\hbar}\frac{1}{\sqrt{4\pi\lambda k_{\mathrm{B}}T}}\left\{|H_{\mathrm{DA}}|^2\exp\left[-\frac{(-\Delta G_0-\lambda)^2}{4\lambda k_{\mathrm{B}}T}\right] + |E_{\mathrm{vac}}\cdot\mu_{\mathrm{DA}}|^2\exp\left[-\frac{(-\Delta G_0-\lambda-\hbar\omega_{\mathrm{c}})^2}{4\lambda k_{\mathrm{B}}T}\right]\right\} \quad (39)$$

Where abbreviation are represented as following, respectively : $\hbar$: Dirac constant, λ : reorganization energy, k_{B} : Boltzmann constant, T : absolute temperature, H : Electronic coupling matrix, ΔG_0 ($= -nF\eta$) : free energy differences, η : overpotential, E_{vac} ($= \sqrt{\frac{\hbar\omega_{\mathrm{c}}}{2\varepsilon_0 V}}$) : vacuum electric field strength, e : elementary charge, ω_{c} : cavity frequency, ε_0: vacuum dielectric constant : transition dipole moment.

Under the strong coupling condition, the reaction kinetic constants for the forward ($k_{\mathrm{f,sc}}$) and backward ($k_{\mathrm{b,sc}}$) processes can be written (hayashi)

$$k_{\mathrm{f,sc}} = k_{\mathrm{f,sc,0}} \exp\left[-\frac{2\alpha F(E-E_0)}{RT}\right] \tag{40}$$

$$k_{\mathrm{b,sc}} = k_{\mathrm{b,sc,0}} \exp\left[\frac{(2-2\alpha)FE}{RT}\right], \tag{41}$$

where $k_{\mathrm{f,sc,0}}$ and $k_{\mathrm{b,sc,0}}$ are the kinetic constants for the forward and backward reactions, respectively, under strong coupling. By utilizing the microkinetic description, multiple electron transfer reactions can understood using hydrogen evolution as a model reaction.

Case 2: strong coupling with the surface electronic species

In the case of coupling with M, Eq. 40 can be used for the microkinetic modeling. The equilibrium between the forward and backward reactions can be expressed as $k_{\mathrm{f,sc}} C_{\mathrm{H2O}}(1-\theta) = k_{\mathrm{b}}\theta$. Therefore, the surface coverage can be written

$$\theta = \frac{KC_{\mathrm{H2O}} \exp\left[-\frac{(1+\alpha)F(E-E_0)}{RT}\right]}{1+KC_{\mathrm{H2O}} \exp\left[-\frac{(1+\alpha)F(E-E_0)}{RT}\right]}. \tag{42}$$

We assume that the forward reaction step (adsorption of hydrogen) can be modified by strong cavity coupling. Therefore, rate equations can be written

$$r_{\mathrm{V,sc}} = k_{\mathrm{V,sc}} C_{\mathrm{H2O}}(1-\theta) = \frac{k_{\mathrm{V}}^0 C_{\mathrm{H2O}} \exp\left[-\frac{2\alpha F(E-E_0)}{RT}\right]}{1+KC_{\mathrm{H2O}} \exp\left[-\frac{(1+\alpha)F(E-E_0)}{RT}\right]} \tag{43}$$

$$r_{\mathrm{H,sc}} = k_{\mathrm{H}} C_{H2O}\theta = \frac{k_{\mathrm{V}}^0 K C_{\mathrm{H2O}}^2 \exp\left[-\frac{(1+2\alpha)F(E-E_0)}{RT}\right]}{1+KC_{\mathrm{H2O}} \exp\left[-\frac{(1+\alpha)F(E-E_0)}{RT}\right]} \tag{44}$$

$$r_{\mathrm{T,sc}} = k_{\mathrm{T}}\theta^2 = k_T \left\{\frac{KC_{\mathrm{H2O}} \exp\left[-\frac{(1+\alpha)F(E-E_0)}{RT}\right]}{1+KC_{\mathrm{H2O}} \exp\left[-\frac{(1+\alpha)F(E-E_0)}{RT}\right]}\right\}^2. \tag{45}$$

Case 3: strong coupling with the surface-adsorbed species

In the case of coupling with the M–H, Eq. 41 can be used for the microkinetic modeling. The equilibrium between the forward and backward reactions can be expressed as $k_{\mathrm{f}} C_{H2O}(1-\theta) = k_{\mathrm{b,sc}}\theta$. Therefore, the surface coverage can be written

$$\theta = \frac{KC_{\mathrm{H2O}} \exp\left[-\frac{(2-\alpha)F(E-E_0)}{RT}\right]}{1+KC_{\mathrm{H2O}} \exp\left[-\frac{(2-\alpha)F(E-E_0)}{RT}\right]}. \tag{46}$$

We assume that the backward reaction step (desorption of hydrogen) can be modified by strong cavity coupling. Therefore, each rate equation can be expressed as the following equations.

$$r_{\mathrm{V}} = k_{\mathrm{V}} C_{\mathrm{H2O}}(1-\theta) = \frac{k_{\mathrm{V}}^0 C_{\mathrm{H2O}} \exp\left[-\frac{\alpha F(E-E_0)}{RT}\right]}{1+KC_{\mathrm{H2O}} \exp\left[-\frac{(2-\alpha)F(E-E_0)}{RT}\right]} \tag{47}$$

$$r_{\mathrm{H}} = k_{\mathrm{H,sc}} C_{\mathrm{H2O}}\theta = \frac{k_{\mathrm{H}}^0 K C_{\mathrm{H2O}}^2 \exp\left[-\frac{2F(E-E_0)}{RT}\right]}{1+KC_{\mathrm{H2O}} \exp\left[-\frac{(2-\alpha)F(E-E_0)}{RT}\right]} \tag{48}$$

$$r_{\mathrm{T}} = k_{\mathrm{T}}\theta^2 = k_{\mathrm{T}}\left\{\frac{KC_{\mathrm{H2O}}\exp\left[-\frac{(2-\alpha)F(E-E_0)}{RT}\right]}{1+KC_{\mathrm{H2O}}\exp\left[-\frac{(2-\alpha)F(E-E_0)}{RT}\right]}\right\}^2 \quad (49)$$

Case 4: strong coupling with both M and M–H

In the case of coupling with both M and M–H species, Eqs. 40 and 41 can be used for the microkinetic modeling. The equilibrium between the forward and backward reactions can be expressed as $k_{\mathrm{f,sc}}C_{\mathrm{H2O}}(1-\theta) = k_{\mathrm{b,sc}}\theta$. Therefore, the surface coverage can be written

$$\theta = \frac{KC_{\mathrm{H2O}}\exp\left[-\frac{2F(E-E_0)}{RT}\right]}{1+KC_{\mathrm{H2O}}\exp\left[-\frac{2F(E-E_0)}{RT}\right]} \quad . \quad (50)$$

We assume that both forward and backward reaction steps (adsorption and desorption of hydrogen) can be modified by strong cavity coupling. Therefore, the rate equations can be written

$$r_{\mathrm{V}} = k_{\mathrm{V}}C_{\mathrm{H2O}}(1-\theta) = \frac{k_{\mathrm{V}}^0 C_{\mathrm{H2O}}\exp\left[-\frac{2\alpha F(E-E_0)}{RT}\right]}{1+KC_{\mathrm{H2O}}\exp\left[-\frac{2F(E-E_0)}{RT}\right]} \quad (51)$$

$$r_{\mathrm{H}} = k_{\mathrm{H,sc}}C_{\mathrm{H2O}}\theta = \frac{k_{\mathrm{H}}^0 KC_{\mathrm{H2O}}^2\exp\left[-\frac{2F(E-E_0)}{RT}\right]}{1+KC_{\mathrm{H2O}}\exp\left[-\frac{(2-\alpha)F(E-E_0)}{RT}\right]} \quad (52)$$

$$r_{\mathrm{T}} = k_{\mathrm{T}}\theta^2 = k_{\mathrm{T}}\left\{\frac{KC_{\mathrm{H2O}}\exp\left[-\frac{2F(E-E_0)}{RT}\right]}{1+KC_{\mathrm{H2O}}\exp\left[-\frac{2F(E-E_0)}{RT}\right]}\right\}^2 \quad (53)$$

By considering all three cases, Tafel behavior can be described as follows. In every case, onset of Tafel behavior occurs at potentials close to the hydrogen adsorption potential, E_0. Therefore, Tafel behavior can be explained by considering either the low- or high-overpotential regions. In all the cases the high-overpotential region for the Volmer step is not considered because it generally applies to the adsorption process, and therefore a high hydrogen surface coverage disturbs the hydrogen adsorption kinetics. A summary of the Tafel slope for Cases 1–4 is shown in Table 1. In general, the Tafel slopes are smaller than those usually obtained for the hydrogen evolution reaction system. This is intriguing because a small Tafel slope requires a small overpotential to achieve a high catalytic current density during the electrochemical reaction.

Table 1. Summary of the Tafel slope (mV/decade) for Cases 1–4.

	Volmer Low η	Heryrovsky Low η	Heryrovsky High η	Tafel Low η	Tafel High η
Case 1	120	40	120	30	∞
Case 2	60	60	120	20	∞
Case 3	120	30	120	20	∞
Case 4	60	30	120	15	∞

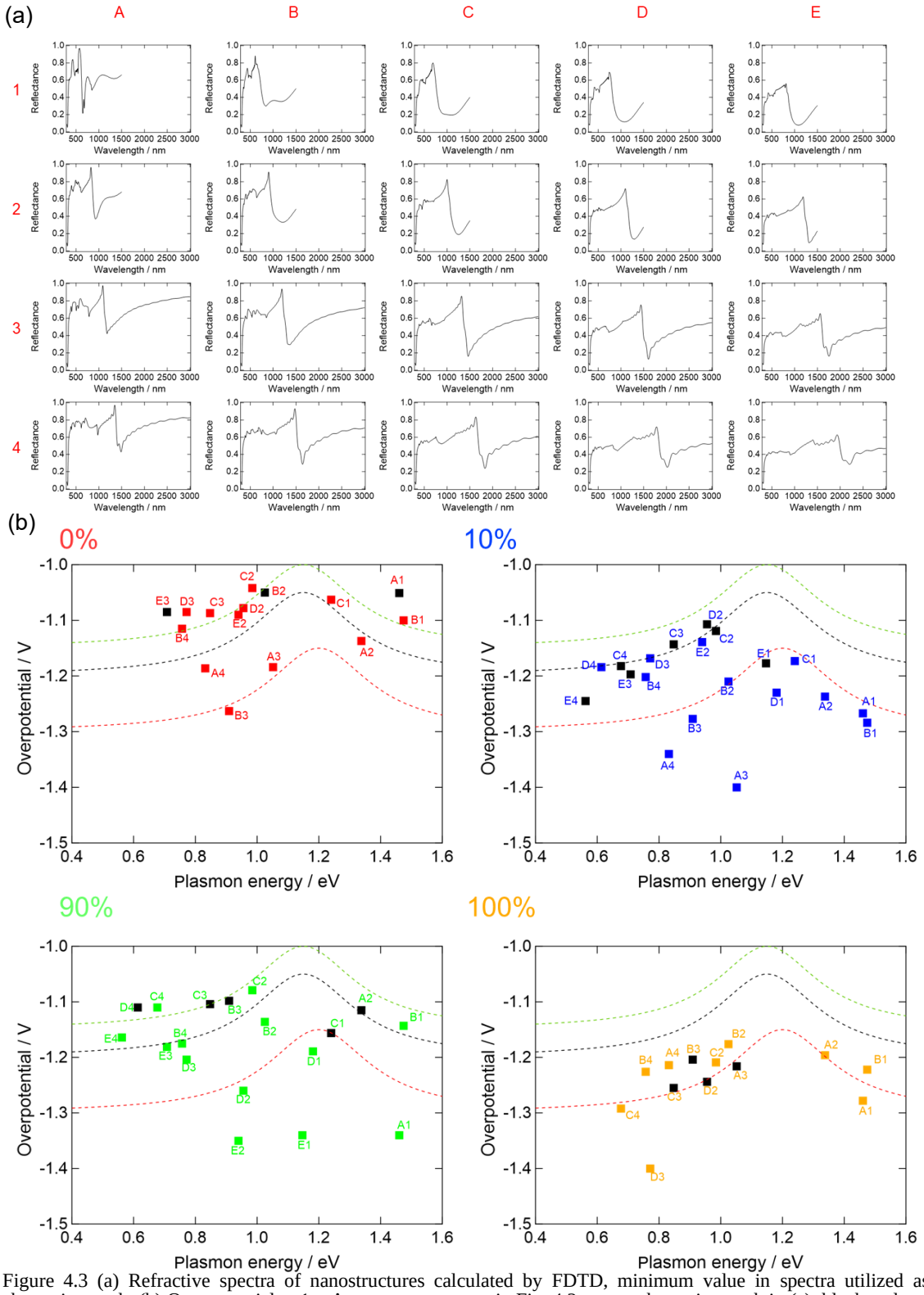

Figure 4.3 (a) Refractive spectra of nanostructures calculated by FDTD, minimum value in spectra utilized as absorption peak, (b) Overpotential at 1 mA on nanostructures in Fig. 4.2 versus absorption peak in (a), black and red dot curve indicate approximation Lorenzen curve in 10% and 100 % respectively. In 0 % and 90% using the same black and red curve.

As mentioned above, when comparing heavy water mixing ratios in a normal electrode, the activity is 0%>10%>90%>100%. In comparison, when comparing the curves with the highest activity for each isotope mixing ratio in Fig. 4.2, the order is 90%>0%>10%>100%. This is thought to be due to the hydrogen bond network structure between the water molecules at the interface as shown in Fig. 4.2 At 0% and 100, there is 100% H_2O and 100% D_2O, so without thinking too hard about it, the network of water molecules on the surface is as shown in Fig. On the other hand, at 10% and 90%, the following equilibrium is established, so it is no longer just H_2O and D_2O.

$$H_2O + D_2O \leftrightarrows 2HDO \qquad (54)$$

This equilibrium constant is 4,[12] so in a 10% solution, the actual ratios of H_2O, D_2O, and HDO are 81% H_2O, 18% HDO, and 1% D_2O, respectively. In contrast, in a 90% solution, the opposite occurs, with 1% H_2O, 18% HDO, and 81% D_2O. Let us consider how HDO molecules form a hydrogen bond network in this case. As a premise, the bond energies of H-O and D-O bonds are different, and the molecular vibrations are also different.[13,14] This has long been known in spectroscopy. From this, it is expected that the hydrogen bonds of H-O…H and D-O…D will be symmetrical and very strong. In contrast, the hydrogen bonds of H-O…D or D-O…H are expected to be weak and not symmetrical. In other words, it is thought that H-O…D or D-O…H are difficult to form in a hydrogen bond network. In other words, it is thought that H-O…H and D-O…D will be formed in the bulk, and the parts that cannot participate in the hydrogen bonds at the interface will face outward.[15] This is shown diagrammatically in Fig. 4.4 at 10% and 90%. In other words, at 10%, the macroscopic ratio is 81% H_2O, 18% HDO, and 1% D_2O, but in the bulk, H_2O and HDO form a hydrogen bond network like H-O...H, with the D of HDO facing outward. In this system, this outward ratio is considered to be the interface between the water and the electrode. Conversely, at 90%, the bulk, DO and HDO form hydrogen bonds like D-O···D, with the H facing the water and electrode interface. From the above, it is not the case that the presence ratio of the solution at the interface in a specific metal nanostructure is simply due to equilibrium. The reason why the activity of 10% and 90% is switched is thought to be because D reacts at 10% and H reacts at 90%. It is thought that the reaction of H or D in each nanostructure can be distinguished by which curve it is on in Fig. 4.3b. However, it is unclear why this happens in the metal nanostructure. At present, it is thought that the enhanced electric field near the metal nanostructure acts to fix the orientation of the hydrogen bond network rather than randomize it.

Fig. 4.3a shows the reflection spectrum by FDTD for each metal nanostructure, and in this case, the wavelength at which this spectrum has a minimum value is considered to be the resonance peak of each metal nanostructure.[3,2] (b) shows the resonance peak on the horizontal axis and the isotope mixing ratio and overvoltage of the metal nanostructure on the vertical axis. This overvoltage indicates the potential when it becomes 1 mA in Fig. 4.2. In other words, it lists the optical information and electrochemical activity of the metal nanostructure. As a characteristic, if I first

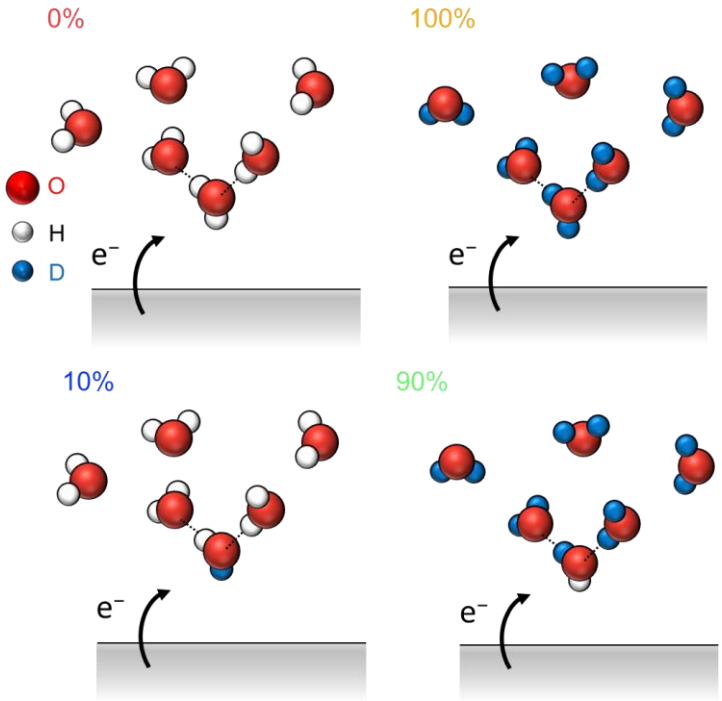

Figure 4.4 Schematic image of water molecule near the nanostructured electrode. In 0% and 100% water molecules have 100% H_2O and D_2O respectively. So that, hydrogen bonds consist of HO-H and DO-D respectively. On the other hand, in 10% and 90% water molecules have 1% D_2O, 81% H_2O, 18% HDO and 1% H_2O, 81% D_2O, 18% HDO, respectively.

discuss the 100% results, fitting the Lorentzian function with the exception of the D3 structure produces a curve like the red dotted line. Since the results other than D3 show a tendency along this curve, it can be inferred that this optical property reflects the activity of the metal nanostructure, and the wavelength of the peak top is about 1.2 eV. The same fitting curve is also drawn as a red dotted line for 0%, 10%, and 90%. In particular, at 10%, many of the results follow this red dotted line, except for structures A3 and A4. Considering the results of the 100% heavy water mixture ratio, I believe that D is reacting in these structures. The black dotted line is a fitting of a different Lorentzian function to the results in the upper left corner of 10%, excluding the points along the red dotted line. Considering the situation, I believe that H is reacting in these structures. The same curve is also drawn in other graphs. From this, I can infer that metal nanostructures react with H or D at 10% and 90%, respectively. Furthermore, there were many more points of higher activity at 0% and 90% than the curve reacting with H. Since this is only for H and not D, I believe that the reaction has been further accelerated and progressed due to quantum tunneling. Since optical properties are not related to quantum tunneling, the peak is the same as that of H, as in the previous discussion.

Finally, when comparing these metal nanostructures, it was found that the structure C2 showed relatively high activity regardless of the isotope mixing ratio, so this structure was fabricated on a GC at a scale of 1 mm × 1 mm and its electrochemical properties were compared. Fig. 4.5 shows the results, with the blue and red lines indicating Ag and Ag plate deposited on a GC, respectively. It can be seen that these two electrodes draw almost similar curves. It was confirmed that the Ag film

peeled off from the GC during HER. As a result, a strange I-V curve was obtained at around −1.5 V. In comparison, the large-area metal nanostructure electrode C2 has a better rise potential and

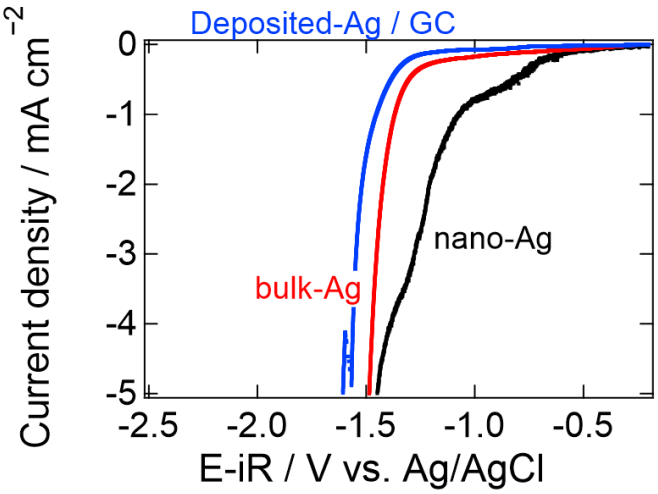

Figure 4.5. LSV for nanostructured (C2) electrode, deposited Ag and Ag plate as a working electrode in 0.25 M Na_2SO_4aq and utilizing Pt black and Ag/AgCl electrode as counter and reference electrode respectively. Black, red and blue curve indicate I-V curve of nanostructured electrode, Ag plate and deposited Ag electrode respectively.

subsequent current value than the other two. It was found that there was a difference of about 0.2 V in the overvoltage required to reach 2 mA cm^{-2}, and it was found that the activity was improved by nanostructuring even in the large-area electrochemical measurement. From this, it was confirmed that the HER activity was improved by nanostructuring in the electrochemical measurement. In addition, it was confirmed that the metal nanostructure was not destroyed when observing the electrode after HER, suggesting the possibility of high durability.

4.4 Conclusions

The bubble observation confirmed that the activity of the metal nanostructured electrode was different from that of the bulk electrode, and that the metal nanostructure was more active. Further detailed analysis revealed that the HER activity differed depending on the isotope mixing ratio of the metal nanostructure, and when comparing the optical properties of the metal nanostructure with those of the metal nanostructure, it was possible to infer that there was a peak in the reactivity. It is particularly important that the peaks are different when H reacts and when D reacts, which suggests that the reactivity of H and D can be controlled by adjusting the optical mode. In addition, the hydrogen bond network in the vicinity of the metal nanostructure is different from that of the bulk electrode, and it is thought that hydrogen bonds via both H and D are less likely to form, which is thought to be the cause of the anomalous isotope effect. Finally, when a metal nanostructured electrode with a large area of 1 mm × 1 mm was fabricated and electrochemical measurements were performed, it was confirmed that it was more active than the bulk electrode, and the overpotential was reduced by 0.2 V @ 2mA cm^{-2}.

4.5 Refeerence

1. Nagarajan, K., Thomas, A. & Ebbesen, T. W. Chemistry under Vibrational Strong Coupling. *J. Am. Chem. Soc.* **143**, 16877–16889 (2021).
2. Semenov, A. & Nitzan, A. Electron transfer in confined electromagnetic fields. *J. Chem. Phys.* **150**, 174122 (2019).
3. Hayashi, T., Fukushima, T. & Murakoshi, K. Role of cavity strong coupling on single electron transfer reaction rate at electrode–electrolyte interface. *J. Chem. Phys.* **161**, (2024).
4. Halas, N. J., Lal, S., Chang, W., Link, S. & Nordlander, P. Plasmons in Strongly Coupled Metallic Nanostructures. *Chem. Rev.* **111**, 3913–3961 (2011).
5. Kravets, V. G., Kabashin, A. V, Barnes, W. L. & Grigorenko, A. N. Plasmonic Surface Lattice Resonances: A Review of Properties and Applications. *Chem. Rev.* **118**, 5912–5951 (2018).
6. Li, C. W. & Kanan, M. W. CO_2 Reduction at Low Overpotential on Cu Electrodes Resulting from the Reduction of Thick Cu_2O Films. *J. Am. Chem. Soc.* **134**, 7231–7234 (2012).
7. Herran, M. *et al.* Plasmonic bimetallic two-dimensional supercrystals for H2 generation. *Nat. Catal.* **6**, 1205–1214 (2023).
8. Park, S. *et al.* Solutal Marangoni effect determines bubble dynamics during electrocatalytic hydrogen evolution. *Nat. Chem.* **15**, 1532–1540 (2023).
9. ANKETELL, J. & LEARNER, R. C. M. Kinetics of Electrolytic Hydrogen and Deuterium Evolution. *Proc. Roy. Soc. London. Ser. A. Math. Phys. Sci.* **256**, 128–144 (1960).
10. Westheimer, F. H. The Magnitude of the Primary Kinetic Isotope Effect for Compounds of Hydrogen and Deuterium. *Chem. Rev.* **61**, 265–273 (1961).
11. Shinagawa, T., Garcia-Esparza, A. T. & Takanabe, K. Insight on Tafel slopes from a microkinetic analysis of aqueous electrocatalysis for energy conversion. *Sci. Rep.* **5**, (2015).
12. Friedman, L. & Shines, V. J. Experimental determination of the disproportionation of hydrogen isotopes in water. *J. Chem. Phys.* **44**, 4639–4640 (1966).
13. Chen, C. L., Bopp, P. & Wolfsberg, M. Evaluation of the equilibrium constant for H_2O+D_2O = 2HDO by direct summation over rotational-vibrational states. *J. Chem. Phys.* **77**, 579–580 (1982).
14. Wolfsberg, M., Massa, A. A. & Pyper, J. W. Effect of vibrational anharmonicity on the isotopic self-exchange equilibria $H_2X+D_2X=2HDX$. *J. Chem. Phys.* **53**, 3138–3146 (1970).
15. Kim, K. & Lee, X. Isotopic enrichment of liquid water during evaporation from water surfaces. *J. Hydrol.* **399**, 364–375 (2011).

5 General Conclusions

In this doctoral thesis, in electrochemical reactions driven under polariton states, I revealed that the reaction was efficiently promoted compared to bulk electrodes. To investigate it I fabricated the nanostructured electrodes controlling optical mode, and I achieved to construct the method to evaluate activity from micrometer scaled experiments. I discovered the distinct difference of activity depending on coupling between reaction intermediates and optical modes of nanostructures. The difference includes overpotential, efficiency and selectivity. Notably, I experimentally confirmed that controlling nanostructures modulates reactivity under polariton states.

In Chapter 1, I introduced the fundamental difficulty in improving activity in HER by developing normal catalysts, and then showed that a breakthrough could be achieved by utilizing the interaction between the optical mode and HER using a metal nanostructure to overcome this difficulty.

In Chapter 2, I constructed a plasmon-induced HER system in which a metal nanostructure is supported on a p-type semiconductor. As a result of investigating the pH dependence, I obtained results showing that the activity was highest under neutral conditions. Considering this result, it is possible that plasmon-induced HER promotes reactions involving H_2O more than reactions involving H^+. This clarified the characteristics of plasmon-induced HER, and I promoted the progress of plasmon-induced chemical reactions using p-type semiconductors, which had been rarely reported.

In Chapter 3, we developed a new method to observe bubble formation and growth during electrochemical HER as a new activity evaluation method, instead of using a current-potential curve that measures the electrochemical activity of the entire electrode. This method successfully calculated Tafel slopes of 120 and 30 mV dec^{-1}, respectively, from experiments using Ag and Pt bulk metal electrodes, values that have long been known in electrochemistry, and the validity of this method was discussed. It was also found that only a small amount of electron transfer was reflected in the early stages of bubble formation, and knowledge was gained about the region in which this electron transfer controls bubble growth.

In Chapter 4, we used the method developed in Chapter 3 to simultaneously observe the HER in multiple types of metal nanostructures on the same substrate, analyzed the images of each, and calculated the activity of each. It was found that the HER activity differed depending on the metal nanostructure and the isotope mixing ratio. A correlation was found between these results and the optical properties of each metal nanostructure calculated by FDTD. It was also suggested that different optical modes may resonate with the reactions of H and D. On the other hand, unlike bulk electrodes, the hydrogen bond network near the interface in metal nanostructured electrodes is different, suggesting the possibility that H-O is more likely to form a hydrogen bond network with

H and D-O is more likely to form a hydrogen bond network with D. This suggests that the chemical reaction coupled to the optical mode is influenced not only by the interface but also by the vicinity of the interface.

Through this doctoral thesis, introducing quantum effects, namely polariton states, into chemical reactions enable to design catalysis which affects a specific elementary step in reactions. This has not been able to be achieved based on many approaches so far in material science fields. It is also possible to promote multi-electron transfer reactions by modulating only the rate determining step. The novelty of this finding is that it is not needed to change catalysis materials depending on the reaction substrate, instead, it can be achieved by only preparing reaction field showing quantum effect interactions with molecules to form polariton states. Therefore, utilizing polariton states could be a novel key approach to control various chemical reaction including electron transfer processes and achieve great reaction efficiency through quantum effects, which open a new possibility for quantum electrochemistry.

Acknowledgement

I would like to express my gratitude to Prof. Dr. Kei Murakoshi for the discussion and teaching in my student life for seven years.

Deep thanks to Lecturer Dr. Hiro Minamimoto for the help even after transferring to Kobe University and Lecturer Dr. Tomohiro Fukushima for experimental and theoretical support and Assistant Prof. Dr. Masaki Itatani for much advice.

Without the cooperation of the laboratory members, I could not attain my research, especially Ryo Osaka, Dr. Nobuaki Oyamada, Takahiro Hayashi and Ryoji Suzuki for experimental lectures and advice, theoretical discussion, analytical help and life advice. I am grateful to Rumi Akiyama, Mariko Yonezawa, Junko Hattori, Hiroko Nishimoto and Chise Kanbara as secretaries in the laboratory.

In my life the family always gives too much support, I would like to express my deepest gratitude to my grandfather, grandmother, father, mother and brother.

Daiki Sato